AGU PUBLICATIONS

JGR

Journal of Geophysical Research: Oceans

RESEARCH ARTICLE

10.1002/2014JC010338

Key Points:
- Ka-band backscattering experiment under different regimes of wavefields
- Empirical model for the 2-D surface spectrum including surface drift current
- Comparison with backscattering from natural surfaces

Correspondence to:
C.-A. Guérin,
guerin@univ-tln.fr

Citation:
Boisot, O., S. Pioch, C. Fatras, G. Caulliez, A. Bringer, P. Borderies, J.-C. Lalaurie, and C.-A. Guérin (2015), Ka-band backscattering from water surface at small incidence: A wind-wave tank study, *J. Geophys. Res. Oceans*, *120*, doi:10.1002/2014JC010338.

Received 24 JUL 2014
Accepted 12 APR 2015
Accepted article online 15 APR 2015

Ka-band backscattering from water surface at small incidence: A wind-wave tank study

Olivier Boisot[1,2], Sébastien Pioch[1], Christophe Fatras[3], Guillemette Caulliez[4], Alexandra Bringer[5], Pierre Borderies[3], Jean-Claude Lalaurie[6], and Charles-Antoine Guérin[1]

[1]Université de Toulon, CNRS, Aix Marseille Université, IRD, MIO UM 110, La Garde, France, [2]CLS/CNES, Toulouse, France, [3]ONERA-DEMR, Toulouse, France, [4]Aix Marseille Université, CNRS, IRD MIO, UM 110, Marseille, France, [5]Electrosciences Laboratory, Columbus, Ohio, USA, [6]CNES, Toulouse, France

Abstract We report on an experiment conducted at the large Pytheas wind-wave facility in Marseille to characterize the Ka-band radar return from water surfaces when observed at small incidence. Simultaneous measurements of capillary-gravity to gravity wave height and slopes and Normalized Radar Cross Section (NRCS) were carried out for various wind speeds and scattering angles. From this data set we construct an empirical two-dimensional wave number spectrum accounting for the surface current to describe water surface motions from decimeter to millimeter scales. Some consistency tests are proposed to validate the surface wave spectrum, which is then incorporated into simple analytical scattering models. The resulting directional NRCS is found in overall good agreement with the experimental values. Comparisons are performed with oceanic models as well as in situ measurements over different types of natural surfaces. The applicability of the present findings to oceanic as well as continental surfaces is discussed.

1. Introduction

Spatial observations of the ocean with microwave instruments have been performed routinely for at least three decades since the launch of SeaSat in 1978, with most of the sensors working in C and Ku bands. However, recent technological progresses have made possible the use of Ka band (35 GHz) which presently attracts a growing interest. The utilization of such a high frequency allows for reduced dimensions of the instruments on board as well as increased resolution and accuracy in the estimation of the sea surface topography. These advantages have been put into practice with the Ka-band wideband altimeter of the successful AltiKa mission or the nonconventional altimeter mission SWOT (Surface Water Ocean Topography, currently in phase A) using a Ka-band radar interferometer [*Durand et al.*, 2010]. However, the physics involved in describing the air-water interface as well as the scattering mechanism at this shorter electromagnetic wavelength is quite different from that considered in usual models, due to the dominant role of the capillary waves as the resonant scatterers. The simulation and interpretation of Ka-band backscattering data over oceanic or continental water surfaces thus require specific studies.

While there is an abundant literature on C, Ku, and X-band radar backscattering from wind-generated water surface waves in tank or oceanic conditions, the use of radar millimeter wavelength range (Ka band) has been far less documented. We found it limited to a few studies performed in airborne [*Masuko et al.*, 1986; *Nekrasov and Hoogeboom*, 2005; *Tanelli et al.*, 2006; *Walsh et al.*, 1998; *Vandemark et al.*, 2004; *Walsh et al.*, 2008; *Fjortoft et al.*, 2014], coastal [*Long*, 2001; *Dyer et al.*, 1974; *Smirnov et al.*, 2003], and wind-wave tank [*Giovanangeli et al.*, 1991; *Keller et al.*, 1995; *Gade et al.*, 1998; *Plant et al.*, 1999, 2004; *Ermakov et al.*, 2010] conditions. These studies have unveiled the specificity of Ka-band radar return in terms of backscattering cross section as well as Doppler signature when compared to lower microwave bands. In particular, wind-wave tank experiments have established the dominant role of bound capillary waves [*Keller et al.*, 1995; *Plant et al.*, 1999, 2004; *Ermakov et al.*, 2010] in the scattering process and its dependence on friction velocity. However, we found no systematic investigation of the absolute level of backscattering cross section at small incidence with respect to the different scattering angles, information which is necessary for the calibration of nonconventional altimeter instruments such as those used in the future SWOT mission. Furthermore, there is a need for specific and tractable wave scattering models to be used in this regime, which requires an accurate statistical description of the water surface at submillimeter scales. Other than the

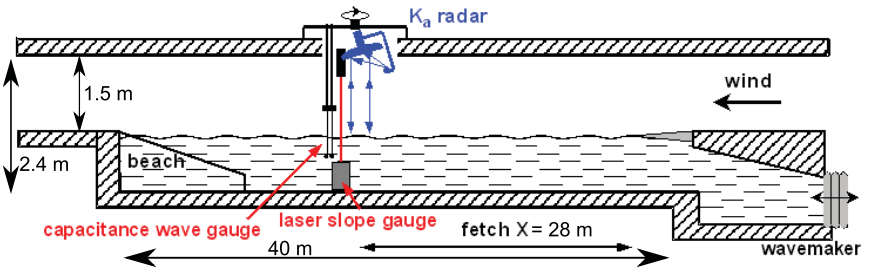

Figure 1. Schematic view of the experimental arrangement and the instrumentation set up in the Pytheas wind-wave facility.

spectral model developed by *Kudryavtsev et al*. [2003a, 2003b], we found no further attempt in the literature to elaborate a statistical representation of the surface which addresses properly the generation of capillary waves and their nonlinear interaction with short gravity waves. The goal of this paper is twofold. First, we report on details on a Ka-band radar experiment in the large wind-wave tank of Marseille-Luminy under a set of wind conditions. This allows to test in a controlled environment the combined surface and scattering model used for the prediction of the near-nadir absolute backscattering radar cross section and to determine in which respect the classical ocean scattering models must be adapted. We propose a methodology to recover the two-dimensional (2-D) wave number spectrum from the combined measurements of the wave height frequency spectrum and up-tank and cross-tank slope frequency spectra with account of the drift current effect, which is found there to be crucial. When combined with the physical optics approximation, the resulting spectrum provides good agreement with the experimental values of the NRCS. We have also tested the simple geometrical optics model and a recent improvement thereof, namely the GO4 model. While the former turns out to be insufficient, the latter allows for an accurate description of the NRCS at the largest wind speeds with only two parameters. These observations also give qualitative insight on the sensitivity of the NRCS to wind speed and scattering geometry. We reveal some unconventional behavior at small wind speeds, such as a nonmonotonic variation of NRCS with the incidence angle. The results are discussed and compared with observations made on continental and oceanic surfaces. Laboratory measurements are found representative of the former in a large extent but can differ deeply from the latter.

The paper is organized as follows. Sections 2 and 3 describe the experimental setup in the wind-wave tank together with the radar system. The basic statistical parameters of the observed wind wave fields are derived in sections 4 and 5. The omnidirectional wave number spectra are given, with a careful inclusion of the effect of drift current in the surface wave dispersion relationship. A specific directional spreading function is constructed, based on the compliance with the observed longitudinal and transverse slope spectra. Section 6 describes the basic scattering model elaborated in this context, namely the physical optics approximation. Sections 7 and 8 are devoted to the experimental assessment of the full scattering model by a systematic comparison of its results with the acquired data basis. At last, section 9 discusses the universality of the results in the light of a comparison with these obtained for continental and ocean surfaces.

2. Experimental Setup

The observations were carried out in the large Pytheas wind-wave facility in Marseille which is made of a 40 m long, 2.6 m wide, and 0.9 m deep water tank and a recirculating airflow channel with a test section of about 1.5 m in height, as described in more details in *Coantic and Bonmarin* [1975] and depicted schematically in Figure 1. Steady winds varying between 1.00 and 13 m s^{-1} are generated by an axial fan located in the recirculation flume. The airflow channel which includes divergent and convergent sections, turbulence grids, and a test section of slightly enlarged height, is specially designed to obtain a low-turbulence homogeneous flow at the entrance of the water tank and a constant-flux air boundary layer over the water surface. At the end of the water tank, a permeable beach damps the wave reflection. The Ka-band radar and instruments for wave measurements were set up at a fixed position located at the 28 m fetch test section of the air channel, which is equipped with an open section in the roof (Figure 2).

The Ka-band radar system assembled by the Office National d'Etudes et de Recherches en Aérospatiale (ONERA) in Toulouse was installed above the open section on two orthogonal rotating plates, each one

Figure 2. View of the wind tunnel, the parabolic antenna, the open waveguide, and the radar source fixed at the end of a sidearm adjusted in a crosswind azimuthal position. The whole radar system is mounted on two rotating plates set up above the tunnel roof opening and surrounded by radar absorbers. The wave gauges and the optical receiver of the slope measuring device immersed in water can be seen on the right side of the radar section.

driven by a step-by-step motor, allowing inclinations up to $\pm 15^{\circ}$ away from nadir and covering $\pm 180^{\circ}$ in azimuth. The system was built around a two-port Vector Network Analyzer (VNA) acting as both RF signal source and receiver. In laboratory conditions, it is impossible to devise an antenna system that would emit at a given incidence in the far-field for which the illuminating field can be approximated by a plane wave. Therefore, we chose to operate in the near-field region of a parabolic dish antenna of diameter $D = 60$ cm with a source located at its focus. At nadir, the antenna is located at 1.75 m above the water surface at rest and is pointed downward illuminating an area located at the center of the water tank. At this distance the divergence of the beam can be neglected (the Fresnel zone starts at $D^2/2\lambda_{EM} \simeq 22$ m) and the electric field distribution across the aperture should be uniform. Both amplitude and phase of the complex incident field on a flat surface have been characterized in an anechoïc chamber (ONERA, Toulouse) prior to the experiment (see below). To determine the geometrical properties of wind waves ruffling the water surface during the radar measurements, a pair of high-resolution capacitance wave probes and a single-point laser slope gauge were set up at the immediate proximity of the radar footprint area in the cross-tank direction (Figure 2). The former are made of two sensitive wires (0.3 mm in diameter) hung vertically by a weight at a distance of 2.7 cm and fixed by means of a thin rod at the top of the air channel. The device used for measuring the up-tank and cross-tank components of the water surface slope is composed of a He-Ne laser mounted vertically above the wind tunnel and an optical receiver immersed in water at a distance of roughly 40 cm from the water surface. After low-pass filtering with a cutoff frequency of 100 Hz and eventual amplification, the wave height and slopes signals were digitized at a frequency rate of 256 Hz and recorded on a PC computer. During the experiments, the wind speed was controlled by means of a Pitot tube located in the middle of the air channel at 22 m fetch and connected to an electronic manometer. At last, the mounts of the probes and the open section of the roof around the parabolic antenna were covered with special Ka-band electromagnetic wave absorbers to avoid spurious reflections due to the experimental environment other than the water surface.

The experiments were performed at six wind speeds ranging between 1.85 and 8 m/s. Side views of surface wavefields developed by wind at 28 m fetch in the large wind-wave facility are given in Figure 3 for three different wind speeds. To better investigate the peculiar radar signature observed at very low wind speeds, special attention was paid for winds below 3 m/s. For a given wind speed, the observations consisted in a series of radar measurements made at regularly spaced incidences (± 1 or $\pm 0.5^{\circ}$) within a preselected range (generally ± 15 or $\pm 5^{\circ}$) for various azimuth angles and three to five wave signal records of 20 min duration made at regular time intervals during the radar measurements. To perform them, the entire radar system was monitored by a PC controlling both the motors and the VNA through a GPIB link. To operate it, a

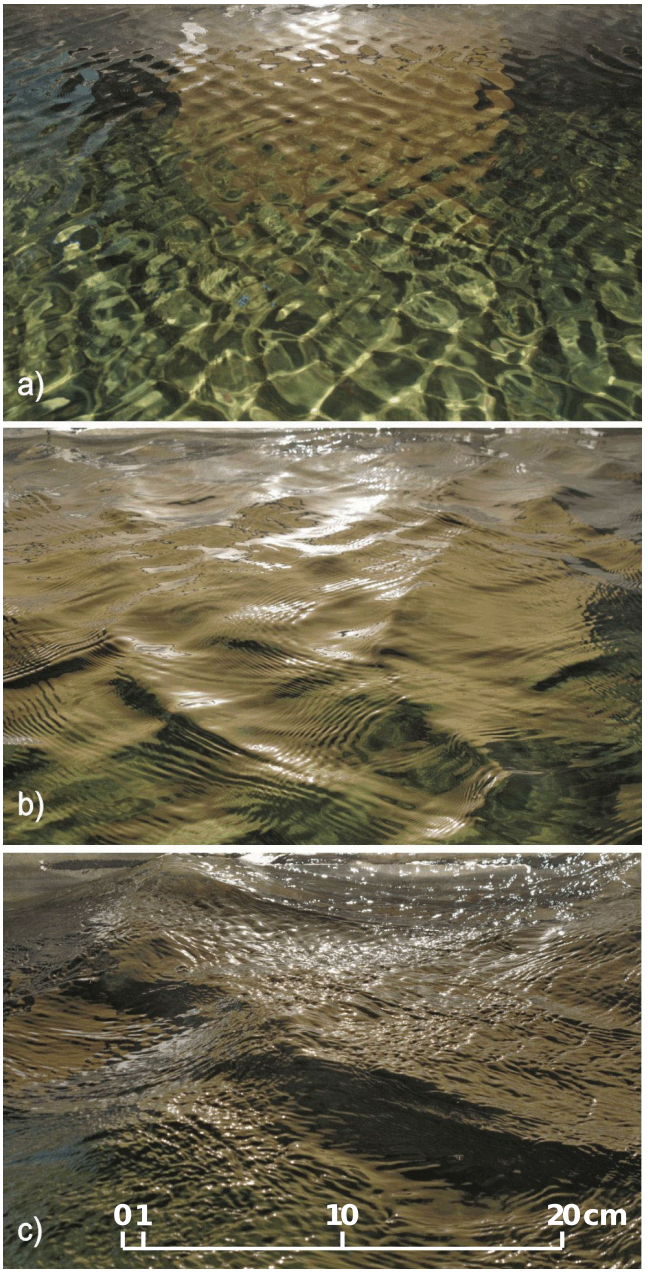

Figure 3. Side view of wind wavefields observed in the large wind-wave tank at 28 m fetch for a wind speed of (a) 2 m/s, (b) 3 m/s, and (c) 8 m/s. The wind blows from the right to the left.

program in Python language was developed. This latter also performs data processing to extract the backscattering coefficient.

3. NRCS Measurement

3.1. Characterization of the Incident Electromagnetic Field

The incident electric field on the illuminated patch has been characterized in the anechoïc chamber of the ONERA by measuring the complex field scattered by small corner reflectors placed at successive locations inside the illumination window and located at approximately 1.15 m from the aperture plane of the antenna. Figure 4 shows the normalized power of the electric field on a flat surface for a corner reflector with an edge 8 cm long. The maximum field is shifted by about 10 cm off the center of the disk. This is probably due to a slight misalignment of the radioelectric axis of the antenna. Cuts of the incident power in different directions show that it can be roughly approximated by a Gaussian illumination window with 80 mm standard deviation. Note that a Gaussian beam with large footprint with respect to the radar wavelength is known [see, e.g., *Soriano et al.*, 2002] to be equivalent (within an overall coefficient of normalization) to a uniform illumination in terms of NRCS, that is, there is no angular distortion of the angular scattering diagram.

The phase of the complex incident electric field on the surface has also been measured. This quantity is difficult to measure in Ka band as it is affected by millimetric variations of the vertical position of the target on the z axis which can be due to nonperfect horizontality of the test table or nonperfectly vertical radio-electric axis. This results in a linear phase bias with respect to the horizontal axis. Once detrended from this linear variation, the phase is found to be normally distributed around zero with a rms of the order of 45°. If we assume that the random phase fluctuations of the incident field can be assimilated to a Gaussian white noise with variance V^2, then this extra phase term can be average independently of roughness in the calculation of the NRCS and leads merely to an overall attenuation factor $\exp(-V^2)$ with respect to the plane wave illumination. For a 45° rms of phase this yields to about 2 dB attenuation which must be added to the calibration factor found in section 3.3 with the radar equation.

3.2. Measurement of the Backscattering Coefficient

A specific procedure has been developed to retrieve the absolute value of the NRCS from the time series of the recorded reflection coefficient. As the target is a fluctuating scene, the time duration for a given

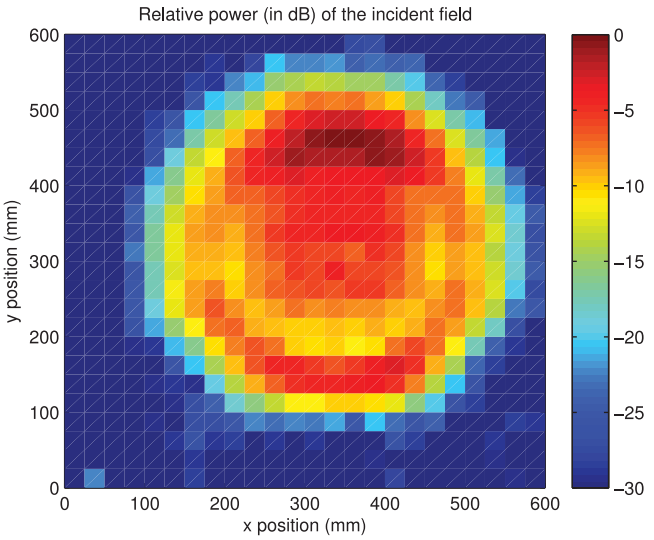

Figure 4. Relative power (in dB) of the incident field on a horizontal plane at 1.15 m from the antenna measured with a 8 cm edge corner reflector.

measurement must be much shorter than the characteristic time of wave motions in order to consider the scene as static. Emission and reception of a continuous electromagnetic wave are done through the S11 port of the VNA. If B is the intermediate frequency (IF) filter width, then the time measurement duration is of order of $1/B$. An IF filter of 10 kHz thus corresponds to a duration of approximately 0.1 ms, during which it is reasonable to assume that the scene is static. The NRCS, denoted σ^0, is proportional to the intensity of the incoherent electromagnetic backscattered field, that is, the variance of the total field. This quantity is estimated from N successive measurements in time, assuming that the water surface roughness at each time corresponds to an independent realization of the same random process. This is actually true if the time lag is of the order of magnitude of a few seconds, that is, much larger than the period of dominant waves. The accuracy in the estimation of the incoherent field is thus of order $1/\sqrt{N}$. It is important to note that in this procedure, the echoes from the static targets (walls and mean flat surface) have no impact on σ^0 estimates because they have no variance in time. In fact, since the N successive radar measurements are independent they contribute only to the total complex field and the average coherent field. Therefore, no specific filtering of these echoes is needed. The records were made by operating the system within three successive loops. The innermost loop involves approximately 500 realizations separated in time by 2 s, while the other two loops concern a scanning in incidence and azimuth angles, respectively.

At this point it is important to discuss the influence of the size of the radar beam footprint on the estimated NRCS. In order to get a scene statistically representative of the random surface roughness, the footprint size has in general to be much larger than the dominant wavelength. Experimental constraints have limited the footprint size to about 35 cm, which is related to the antenna diameter in the near field. For the highest wind speeds, the latter is of the same order of magnitude or even smaller than the dominant wavelength. However, the classical two-scale picture shows that the missing large scales are included through their tilting effect in the time-averaging process of the reflected field, provided the time series is sufficiently long. Hence, it is expected that the convergence to the statistical NRCS be slower at larger winds. Owing to the large number of incidence and azimuth angle configurations to investigate at each wind speed, the duration of individual time records for σ^0 estimates was fixed to 1000 s. To provide additional independent samples in the estimation of the NRCS, a further average has been applied to the σ^0 calculated for every frequency component in the frequency ramp of the radar signal (50 frequency steps from 34.0 to 35.0 GHz), assuming the change of NRCS resulting from the variation of frequency negligible for such a narrow bandwidth.

3.3. Calibration Procedure

For retrieving the backscattering coefficient from measurements of the incoherent electromagnetic wavefield, the radar system must be calibrated carefully. Let us assume an incident complex field with constant amplitude on the illuminated rough surface at a given angle of incidence. This assumption is reasonable if the distance between the antenna and the water surface is less than 22 m since the latter is in the near-field region of the antenna in which the field can be assumed tubular, that is, uniform across the aperture. On the other hand, the incoherent backscattered field received on the antenna is in the far field of the ripples of the surface. The radar equation applied to this configuration thus provides the following estimate for the backscattered power (P_r) received by the antenna:

$$P_r = \frac{A_a}{4\pi D_w^2}(\sigma^0 A_w)\, eP_i, \tag{1}$$

where P_i is the emitted power density and e the antenna efficiency, A_a is the antenna surface, $A_w = A_a/\cos\theta_i$ is the area of the water surface which is illuminated by the near-field tubular beam and thus equal to the projected antenna surface (θ_i is the incidence angle) and D_w is the distance between the antenna and the intercepted part of the rough surface. We recall that σ^0 is the (dimensionless) NRCS of the water surface at the given incidence. Let us now consider a reference target. If the system is illuminating a trilateral corner reflector with a known radar cross section σ_t at a distance D_t from the antenna, the received power is (assuming the antenna in the far field of the corner reflector):

$$P_t = \frac{A_a}{4\pi\cos\theta_i D_t^2}\sigma_t\, eP_i. \tag{2}$$

We may therefore estimate the power received from the water surface by a comparison with the power received from the corner reflector set up inside the tank at the same distance as the water surface (1.75 m). This leads to the relationship:

$$\sigma^0 = \frac{P_r}{P_t}\frac{D_w^2}{D_t^2}\frac{\sigma_t}{A_w}. \tag{3}$$

Note that the measurement of the reference power P_t need not be repeated every time for calibration and may be done only once in laboratory. This was done with a 8 cm edge corner reflector. As this target is steady, its measurement may use time domain filtering [*Ulaby et al.*, 1990] for eliminating unwanted echoes.

As seen in section 3.1, the field distribution is not perfectly equiamplitude and equiphase on the illuminated area and the power scattered by the corner reflector may vary from one location to another inside the surface as shown in Figure 4. This is certainly due to the limited size of the antenna with respect to the wavelength, which is imposed by the wind tunnel constraints. Nevertheless, it can be shown by dividing the illuminated area in small pixels of constant illumination that (3) remains valid for a nonuniform illumination provided the power received by the water surface ($P_t A_w$) is replaced by the integrated power over the surface. A detailed analysis of the possible sources of errors in the estimation of the calibration coefficient gives a maximum possible bias of ± 1.1 dB due to the technique itself and the cumulated sources of errors (± 0.15 dB due to ± 2.5 cm inaccuracy on distances, ± 0.25 dB on target radar cross section, ± 0.65 dB on the average emitted density P_i) and an additional relative fluctuation of 0.3 dB in the estimation of the incoherent field from a finite number (~ 500) of independent sample surfaces. This gives an overall absolute error less than ± 1.4 dB. Note that the relative error (that is after correction of an eventual bias) is less than 0.5 dB.

4. Statistical Parameters of the Water Surface

Modeling the radar return from the water surface requires an accurate statistical description of the surface wave roughness. For this we choose a Cartesian coordinate system (x, y, z) in which z is the vertical axis and (x, y) the mean plane of the water surface. The excursion of the water surface about its mean plane is described by a random field $z = \eta(\boldsymbol{r}, t)$ depending on the horizontal position $\boldsymbol{r} = (x, y)$ and the time t. The wave field is assumed to be stationary (that is statistically invariant under translation in time or space) as well as ergodic in both variables, which means that the ensemble average $\langle\cdot\rangle$ of the process and related quantities can be obtained through temporal as well as spatial averages.

The root mean square (rms) elevation is given by the ensemble average $\langle\eta^2\rangle^{1/2}$ and the significant height (H_s) is 4 times this value. It can be obtained by the average in time of the wave height signal measured at a single location. The longitudinal, transverse, and total mean square slope (mss) are, respectively, given by:

$$s_x^2 = \langle(\partial_x\eta)^2\rangle,\ s_y^2 = \langle(\partial_y\eta)^2\rangle,\ s^2 = s_x^2 + s_y^2. \tag{4}$$

They can be obtained from the instantaneous wave slope measurements with the laser gauge. The wave frequency spectra $S(f)$ are obtained with the usual periodogram technique using time series of elevation

measure at a single point of the water surface. As well known, they have a pronounced maximum (S_p) at the so-called peak frequency (f_p) related to the dominant waves developed by wind along the basin. The spatial properties of the random process are described by the autocorrelation function $\rho(\boldsymbol{r})$ given by:

$$\rho(\boldsymbol{r}) = \langle \eta(\mathbf{r}, t)\eta(\mathbf{0}, t)\rangle, \tag{5}$$

or, equivalently, the structure function ($S_2(\boldsymbol{r})$) given by:

$$S_2(\mathbf{r}) = \langle (\eta(\mathbf{r}) - \eta(\mathbf{0}))^2 \rangle = 2(\rho(\mathbf{0}) - \rho(\mathbf{r})), \tag{6}$$

where $\boldsymbol{r}$ is the space vector measuring the distance between two points of the horizontal plane. The wave number spectrum $\Psi(\boldsymbol{k})$ can be defined as the Fourier transform of the autocorrelation function as follows:

$$\Psi(\boldsymbol{k}) = \frac{1}{(2\pi)^2} \int d\boldsymbol{r}\, e^{i\mathbf{k}\cdot\mathbf{r}} \rho(\boldsymbol{r}). \tag{7}$$

There was no direct observation of these spatial quantities, which then must be inferred from other measurements such as wave elevation and slope frequency spectra (see hereafter).

A series of measurements has been conducted for different wind speeds ranging from 1.85 to 8 m/s. The related basic wave statistical parameters are reported in Table 1.

The corresponding wave frequency spectra at the different wind speeds are shown in Figure 5. These spectra have been renormalized by the peak frequency (f_p) and the maximal spectral energy density ($S(f_p)$), that is, $S(f/f_p)/S_p$.

The various wave spectra exhibit very similar features, that is, a sharp peak around the dominant frequency and for winds above 3 m/s a power law decay in the high-frequency wave range. At such large fetch (28 m) and winds higher than 3 m/s, the dominant peak is located in the gravity wave range and so the wave spectra observed around the peak at various winds exhibit a universal behavior related to the self-similar nature of dominant wind wave fields at such scales. This can be evidenced by a spectrum renormalization using the peak frequency f_p and the spectral peak energy S_p (Figure 5). We found that the shape of this peak is well described by a JONSWAP spectrum [*Hasselmann et al.*, 1973] with appropriate parameters. Note also that the dominant peak associated with gravity-capillarity wave fields observed at winds below 3 m/s does not differ from this spectral model.

The high-frequency range starting from $2f_p$ is more difficult to parameterize and the classically employed power law approximation $S(f) \sim f^{-\nu}$ proposed by *Phillips* [1977] to describe the spectral tail of gravity waves seems to be too crude in the present case, except at the largest wind speeds where an approximate f^{-3} behavior is found in the tail of the spectrum. This is slightly different from the observations of wind wave fields reported in *Zavadsky et al.* [2013], where the spectral tail could be fitted with a power law decrease, with a varying exponent ranging from 3.1 to 3.74 as the fetch is varied from 1 to 3.8 m. This difference with our observations is attributed to the much shorter fetches used in this last study. The second and higher harmonics of the peak frequency are visible at smaller winds and less pronounced at larger winds. Note the plateau observed at very low wave frequency below the dominant peak which might be produced by the slow variations of the mean water level induced by the random development of large-scale dominant wave groups.

Table 1. Basic Statistical Parameters of the Water Surface Roughness Observed for the Different Wind Conditions[a]

U	f_p	H_s	s_x^2	s_y^2	s^2
1.85	4.91	0.26	0.339	0.063	0.402
2	4.34	0.39	0.560	0.113	0.673
2.3	3.63	0.66	0.878	0.214	1.09
3	2.91	1.10	1.10	0.276	1.38
6	1.91	3.13	2.34	0.936	3.27
8	1.84	4.43	3.48	1.64	5.12

[a]The wind speed (U) is given in m/s, the peak frequency (f_p) in Hz, the significant height (H_s) in cm, and the mss (s_x^2, s_y^2, s^2) in %. These quantities are averaged over the whole set of time sequences recorded at a given wind speed.

5. Two-Dimensional Wave Number Spectra

5.1. The Issue of the Short-Wave Spectrum

The derivation of the full two-dimensional wave number spectrum from the frequency spectrum when waves propagate in the presence of either current or long waves has a long history and still today remains a difficult question [e.g., *Hughes*, 1978; *Hara*

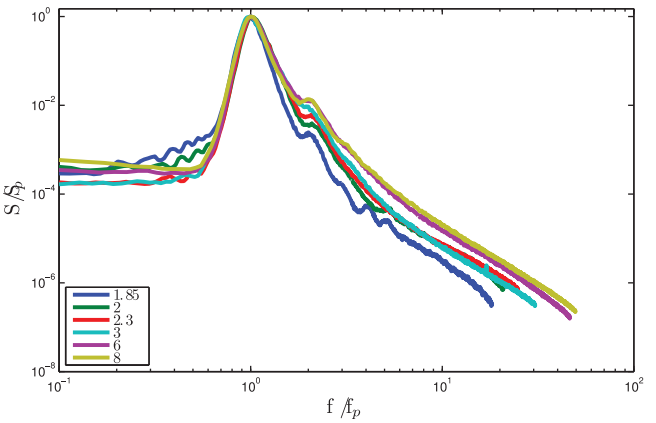

Figure 5. Frequency spectra of the surface wave height observed in the large wind-wave tank at 28 m fetch and six different wind speeds (1.8, 2, 2.3, 3, 6, and 8 m/s). The different spectra have been renormalized by the peak frequency (f_p) and the maximal spectral energy density ($S(f_p)$), that is, $S(f/f_p)/S_p$.

et al., 1994; *Hwang*, 2006; *Plant*, 2015]. It must in general be complemented by other types of measurements (see *Hwang et al*. [2013] for a recent review). As it is well known, the dispersion relation of short waves is affected not only by the mean drift current but also by the Doppler shift of short waves arising from the advection of dominant wave orbital velocities. This raises two related issues, one pertaining to the interpretation of the high-frequency spectrum and the other to the use of the frequency-wave number linear dispersion relation. However, in the present experiment dominant wind waves remain quite short, as opposed for example to the tank experiment cited in *Hwang* [2006] where longer waves are mechanically generated or to in situ measurements used by *Hara et al*. [1994] and *Plant* [2015]. We provide hereafter some heuristic arguments to support the fact that the dominant wave artifact has no significant impact in our analysis of the short-wave spectrum. For simplicity we ignore the directional effects and make a one-dimensional analysis in the main direction of propagation, that is, the direction of wind speed (where the advection phenomena are most pronounced). The apparent spatial frequency k corresponding to a given frequency ω differs from the short-wave intrinsic wave number k_i (including the mean drift current u_c) by a quantity proportional to the maximal wave-induced orbital velocity u_{ad}:

$$\omega = k(c + u_c + u_{ad}\cos\Phi) = k_i(c + u_c), \tag{8}$$

where c is the (free) short-wave celerity and Φ is the phase in the long-wave orbital cycle. Assuming that the ratio

$$\varepsilon = \frac{u_{ad}}{c + u_c} \tag{9}$$

is much smaller than one we may approximate

$$\Delta k = k - k_i \simeq \varepsilon \cos\Phi\, k_i. \tag{10}$$

Because the wave number spectrum is not a linear fluctuation, the symmetric variations of the apparent frequency around a given intrinsic frequency induce a bias in the estimated average wave number spectrum:

$$\Delta\Psi = \Psi(k) - \Psi(k_i) \simeq \frac{1}{2}\langle(\Delta k)^2\rangle\Psi''(k_i), \tag{11}$$

where Ψ'' denotes the second derivative with respect to k. This leads to the following relative variation of the wave number spectrum:

$$\frac{\Delta\Psi}{\Psi} = \frac{1}{4}\varepsilon^2\left(k_i^2\frac{\Psi''(k_i)}{\Psi(k_i)}\right). \tag{12}$$

In the short-wave spectral range the frequency spectrum follows approximately a ω^{-3} behavior at the largest wind speeds implying a $k^{-\nu}$ decay with $1.5 \leq \nu \leq 2$ for the wave number spectrum. This sets a maximum value of 6 for the right-hand side factor arising from the spectral curvature. On the other hand, the maximal orbital speed u_{ad} of long wave can be estimated from the relation $u_{ad} = s_{dom}c_{dom}$, where $s_{dom} = \sqrt{mss_{dom}}$ is the mean steepness associated to the dominant wave and c_{dom} is the phase speed of the dominant wave. The quantity mss_{dom} has been estimated by integration of the laser slope spectrum between 0.5 f_p and 1.5f_p while the dominant wave phase speed has been estimated by using a cross-correlation method between two neighbor wave gauge signals. For the highest wind speed (8 m/s) corresponding to the largest

advection current we found $u_{ad}=0.14\times100=14$ cm/s and a mean drift current u_c of the order of 14 cm/s as well. In the less favorable case where the short-wave celerity is taken at its minimum (23 cm/s) this leads to an estimation $\varepsilon=0.38$ and $\Delta\Psi/\Psi \leq 0.2$. Such a relative variation of the wave number spectrum around the minimum phase wave number (363 rad/m) would induce a variation of at most 1 dB for the scattered power from the resonant Bragg wave. However, at low angles and for the largest wind speeds, the NRCS has less sensibility to the resonant frequency and is dominantly affected by larger waves for which the bias induced by dominant wave orbital motion is much smaller. A first partial conclusion is that it is meaningful to estimate the short-wave wave number spectrum from short-wave frequency spectrum using the intrinsic dispersion relationship of capillary-gravity waves in presence of a mean current, that is,

$$(\omega-\boldsymbol{k}\cdot\boldsymbol{u})^2=gk+\gamma_0 k^3, \tag{13}$$

with $g=9.81$ m/s the gravitational constant, $\gamma_0=7.44\cdot10^{-5}$ m^3/s^2 the surface tension coefficient for freshwater, and u the surface current. However, it remains to verify that the dominant wave orbital velocity has still no impact on the dispersion relationship, an issue which has been investigated in detail in *Hwang* [2006] by considering the variation of the Jacobian in the $k-\omega$ transformation. Again, we provide heuristic arguments in the case of a one-dimensional flow. The change of variable $\omega \rightarrow k$ involves the Jacobian

$$J=\left|\frac{dk}{d\omega}\right|=|c_g+u_{ad}\cos\Phi+u_c|^{-1}, \tag{14}$$

where c_g is the group velocity associated to the wave number k in absence of current. The group velocity of capillary-gravity waves is of the order $c_g \simeq \frac{3}{2}c_p$ with $c_p \sim 23$ cm/s at least and we therefore have for the Jacobian averaged over many orbital cycles for the highest wind speed:

$$(c_g+u_c)\times\langle J\rangle \simeq \langle(1-0.3\cos\Phi+0.045\cos^2\Phi+\ldots)\rangle \simeq 1.022. \tag{15}$$

Hence, the contribution of the orbital current induces a relative variation of about 2% in the dispersion relationship and will thus be neglected. In view of the previous considerations and the behavior of the dispersion relation estimated experimentally from wave amplitude and slope spectra (see Figure 7) we will assume that the wave fields are essentially monodispersive, which implies a one-to-one correspondence between spatial and temporal scales. To model the latter, we will only take into account a constant drift current.

5.2. Estimation of the Directional Spectrum

From now on we assume a constant surface current $\boldsymbol{u}_c$ aligned with the wind direction (x axis) and homogeneous in the crosswise direction. Any wave vector $\boldsymbol{k}=\boldsymbol{k}(f,\phi)$ together with its norm $k(f,\phi)$ is thus uniquely specified by a frequency f and a direction angle ϕ referred to the x axis. The variance of the surface elevation can be expressed with respect to either the frequency or wave number spectrum:

$$\langle\eta^2\rangle=\int d\boldsymbol{k}\,\Psi(\boldsymbol{k})=\int_0^\infty df\,S(f). \tag{16}$$

Denoting $J(f,\phi)$ the Jacobian corresponding to the change of variable $\boldsymbol{k}\rightarrow(f,\phi)$ we thus have the identity:

$$S(f)=\int_0^{2\pi} d\phi\,\Psi(f,\phi)J(f,\phi), \tag{17}$$

with the understanding $\Psi(f,\phi)=\Psi(\boldsymbol{k}(f,\phi))$. We now decompose the two-dimensional wave number spectrum into an omnidirectional part ($\Psi_0(k)$) and an angular spreading function ($Y(k,\phi)$) according to the expression:

$$\Psi(\boldsymbol{k})=\Psi(k,\phi)=\frac{1}{k}\Psi_0(k)Y(k,\phi), \tag{18}$$

with the normalization condition:

$$\int_0^{2\pi} d\phi\,Y(k,\phi)=1. \tag{19}$$

As we shall see the relation (17) allows the inversion of the omnidirectional spectrum. To evaluate the angular spreading function $Y(k,\phi)$ we rely on the longitudinal ($S_{\parallel}(f)$) and transverse ($S_{\perp}(f)$) slope frequency spectra obtained from the wave slope measurements in the alongwind and crosswind direction, respectively. By definition of the directional slopes we can write:

$$s_x^2=\int_0^\infty df\, S_{\parallel}(f),\; s_y^2=\int_0^\infty df\, S_{\perp}(f). \tag{20}$$

The variances of slopes are also given by the partial second moments of the wave number spectrum, that are:

$$\begin{aligned} s_x^2&=\int_0^\infty df\int_0^{2\pi} d\phi\, k^2(f,\phi)\cos^2\phi\,\Psi(f,\phi)J(f,\phi),\\ s_y^2&=\int_0^\infty df\int_0^{2\pi} d\phi\, k^2(f,\phi)\sin^2\phi\,\Psi(f,\phi)J(f,\phi). \end{aligned} \tag{21}$$

This provides the following identification:

$$\begin{aligned} S_{\parallel}(f)&=\int_0^{2\pi} d\phi\, k^2(f,\phi)\cos^2\phi\Psi(f,\phi)J(f,\phi),\\ S_{\perp}(f)&=\int_0^{2\pi} d\phi\, k^2(f,\phi)\sin^2\phi\Psi(f,\phi)J(f,\phi). \end{aligned} \tag{22}$$

In order to characterize the spreading function we introduce the upwind/crosswind ratio $D(f)$:

$$D(f)=\frac{S_{\parallel}(f)-S_{\perp}(f)}{S_{\parallel}(f)+S_{\perp}(f)}. \tag{23}$$

This ratio quantifies the anisotropy of the wave field. Its ranges from 1 for long-crested surface waves propagating in the wind direction to 0 for fully isotropic wavefield. It can be evaluated directly from the measured frequency wave slope spectra as shown in Figure 6 for various winds. This ratio exhibits a well-defined peak at the dominant frequency. In this range of wind speeds, its level varies only slightly, being quasi-constant for the three smallest wind speeds, increasing a little at 3 m/s and then decreasing at higher wind speeds. This slow variation, however, results from a drastic change in the directional properties of the respective dominant wind wave fields, evolving from well-organized rhombic wave patterns formed by two oblique waves propagating at $\pm 30^{\circ}$ to the wind direction as shown in Figure 3 at very small wind speeds to more randomly distributed short-crested wave patterns propagating mostly in the wind direction (see *Caulliez and Collard* [1999] for more details). Correspondingly, at high frequencies, we can distinguish two different trends in the behavior of the wave field anisotropy. At very small wind speeds, D(f) values observed just above 10 Hz are very similar to the dominant wave ones, except above 40–50 Hz where this ratio starts to increase continuously. This reflects the fact that the parasitic bound waves generated at the crest of dominant waves by a nonlinear instability mechanism as described theoretically by, e.g., *Tsai and Hung* [2007, 2010] have fundamentally the same three-dimensional features as the carrier waves and propagate at the same phase speed [*Caulliez*, 2013]. In that respect, the D(f) increase observed above 50 Hz may result from the fact that the ripple harmonics in the crosswind direction are more rapidly damped than these in the

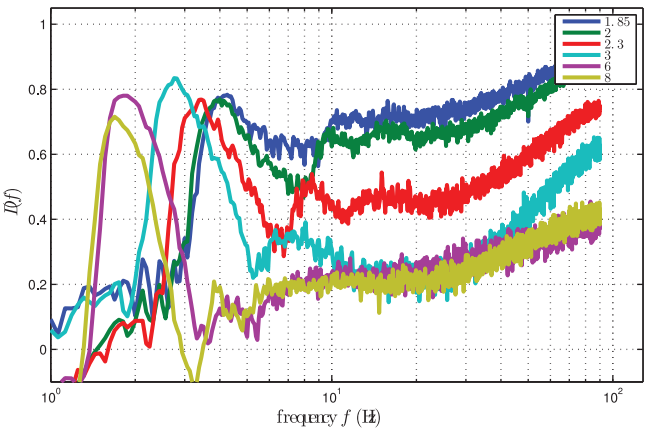

Figure 6. Upwind/crosswind ratio $D(f)$ of slope frequency spectra estimated for the same wind and fetch conditions as in Figure 5.

wind direction, the energy of the latter being directly supplied by wind. At 3 m/s, capillary-gravity ripples generated by short-crested wave microbreaking or even directly by wind (at higher winds) can propagate freely at the water surface. These waves ranging in the frequency domain around and above 10 Hz exhibit a more isotropic spreading compared to bound capillary waves observed at small winds. Above 50 Hz, the increase in D(f) is very likely due to a similar effect as this mentioned previously. From this viewpoint, the wave field observed at 2.3 m/s wind speed appears as an intermediate case between these two types of wave fields with distinctive features.

The contrast function $D(f)$ can be expressed in term of the two-dimensional wave number spectrum, in view of (22):

$$D(f)=\frac{\int_0^{2\pi} d\phi\, k^2(f,\phi)(2\cos^2\phi-1)\Psi(f,\phi)J(f,\phi)}{\int_0^{2\pi} d\phi\, k^2(f,\phi)\Psi(f,\phi)J(f,\phi)}. \tag{24}$$

To proceed further we must now assume a specific shape of the spreading function $Y(k,\phi)$. The most general form is a Fourier expansion with respect to the azimuthal pair harmonics:

$$Y(k,\phi)=\frac{1}{2\pi}(1+\Delta_2(k)\cos(2\phi)+\Delta_4(k)\cos(4\phi)+\ldots). \tag{25}$$

When reduced to the second harmonic it coincides with the popular form proposed by *Elfouhaily et al.* [1997]:

$$Y(k,\phi)=\frac{1}{2\pi}(1+\Delta(k)\cos(2\phi)). \tag{26}$$

The advantage of this formulation is that the function $\Delta(k)$ can be simply inferred from the ratio of measurable quantities such as the wave number spectrum, the directional slope spectra, or the directional mss in two orthogonal directions. We have in particular

$$\frac{s_x^2}{s_y^2}=\frac{\int dk\Psi_0(k)k^2(1+\Delta(k)/2)}{\int dk\Psi_0(k)k^2(1-\Delta(k)/2)}, \tag{27}$$

for the partial or total directional mss (depending on the integration bounds). However, since $\Delta(k)$ should be smaller than unity to ensure the positivity of the spectrum, this limits the ratio of upwind and crosswind partial or total mss to a maximum value of 3. The observed ratio of mss in the wave tank is far beyond this value as seen in Table 1 and therefore excludes the use of the biharmonic spreading function (26). On the other hand, the determination of higher azimuthal harmonics in (25) cannot be achieved with the sole knowledge of the directional slopes and requires higher moments of the directional spectrum. To obtain a more contrasted wave amplitude between the longitudinal and transverse direction with a spreading function which can still be determined from the directional slopes we have devised an ad hoc azimuthal dependence:

$$Y(k,\phi)=\left(\int_0^{2\pi} d\phi\, e^{-\alpha(k)\sin^2\phi}\right)^{-1} e^{-\alpha(k)\sin^2\phi}, \tag{28}$$

where the function $\alpha(k)$ has to be adjusted with the observations. Note that this function which depicts an unimodal angular distribution pointed toward the wind direction appears appropriate for modeling wave fields observed above 3 m/s. At lower wind speeds for rhombic wind wave fields, it should be regarded only as a very first approximation.

To estimate the omnidirectional (Ψ_0) and directional part (Y) of the wave number spectrum, we first discard the current thus assuming $\boldsymbol{u}_c=\boldsymbol{0}$. We denote $\boldsymbol{k}_0(f,\phi)$ and $k_0(f)$ the corresponding dispersion relations for the wave vector and its norm (this latter now depending on the sole frequency). Under these circumstances the Jacobian is merely given by:

$$J(f,\phi)=J(f)=k_0(f)\frac{dk_0(f)}{df}, \tag{29}$$

where $k_0(f)$ is the solution of the third-order equation:

$$gk+\gamma_0 k^3-(2\pi f)^2=0. \tag{30}$$

It follows from (17) the simple relation between the frequency spectrum and the omnidirectional wave number spectrum:

$$S(f)=\Psi_0(k_0(f))\frac{dk_0(f)}{df}, \tag{31}$$

which is equivalent to the more classical relation:

$$\Psi_0(k)=S(f(k))\frac{df(k)}{dk}, \tag{32}$$

that is explicitly:

$$\Psi_0(k)=\frac{1}{4\pi}\frac{g+3\gamma_0 k^2}{(gk+\gamma_0 k^3)^{1/2}}S(f(k)). \tag{33}$$

In view of equation (29) the upwind/crosswind ratio given by (24) simplifies to:

$$D(f)=\int_0^{2\pi} d\phi\,(2\cos^2\phi-1)Y(k,\phi), \tag{34}$$

where k is implicitly given by $k=k_0(f)$.

For the biharmonic spreading function (26) this leads to the simple relation:

$$D(f)=\frac{1}{2}\Delta(k), \tag{35}$$

showing that this formulation is not acceptable as soon as $D(f)\geq 1/2$. For the chosen functional form (28), it leads to an indirect relation:

$$D(f)=\frac{\int_0^{2\pi} d\phi\,(2\cos^2\phi-1)\mathrm{e}^{-\alpha(k)\sin^2\phi}}{\int_0^{2\pi} d\phi\,\mathrm{e}^{-\alpha(k)\sin^2\phi}}=:F(\alpha(k)). \tag{36}$$

The function $F(\alpha)$ must be evaluated numerically. It is an increasing function of α with $F(0)=0$ and $F(\infty)=1$.

In the presence of current ($u_c\neq 0$), the Jacobian J follows the same expression (29) with an angular dependence:

$$J(f,\phi)=k(f,\phi)\frac{dk}{df}(f,\phi) \tag{37}$$

and from (17) the frequency spectrum has the form:

$$S(f)=\int_0^{2\pi} d\phi\,\Psi_0(k(f,\phi))Y(k(f,\phi),\phi)\frac{dk}{df}(f,\phi). \tag{38}$$

For very directional waves about the wind direction, as it is the case for the dominant waves and its bound capillary waves, the main contribution to the integral originates from the vicinity of $\phi=0$, so we may approximate $k(f,\phi)\simeq k(f,0)$. This leads to the modified relationship between the two spectra:

$$S(f)\simeq\Psi_0(k(f,0))\frac{dk}{df}(f,0), \tag{39}$$

where $k(f,0)$ is the root of the third order equation:

$$(2\pi f - k u_c)^2 = gk + \gamma_0 k^3. \tag{40}$$

This solution is given explicitly by means of Cardan formula:

$$k(f,0) = \left(-\frac{q}{2} + \sqrt{\delta}\right)^{1/3} + \left(-\frac{q}{2} - \sqrt{\delta}\right)^{1/3} + \frac{u_c^2}{3\gamma_0}, \tag{41}$$

with

$$\begin{aligned} \delta &= \frac{q^2}{4} + \frac{p^3}{27} > 0, \\ p &= \frac{1}{\gamma_0}\left[g + 4\pi f u_c - \frac{u_c^4}{3\gamma_0}\right], \\ q &= \frac{1}{\gamma_0}\left[\frac{-2u_c^6}{27\gamma_0^2} + \frac{u_c^2}{3\gamma_0}(g + 4\pi f u_c) - (2\pi f)^2\right]. \end{aligned} \tag{42}$$

Due to the abrupt variations of the frequency spectrum on both sides of the spectral peak, the introduction of the current is crucial in determining the value of the dominant wave number which is downshifted with respect to its current-free position. We also found that accounting for the current in the dispersion relation has an important impact on the high-frequency part of the wave number spectrum since it leads to a shifting of the curvature bump observed in the capillary range to higher frequencies. Since the spreading function has a smooth dependence on the wave number, we neglected the effect of current in its estimation; that is, we used formula (36) for the determination of the parameter α_k. The inversion of the omnidirectional wave spectrum from equation (39) requires the a priori knowledge of the current u_c. Now the usual rule of thumb which expresses the latter as a fraction of wind speed provides only a rough estimation. To obtain a more precise estimate of the current we proceeded by validating a posteriori the value which, when used in the calculation of the omnidirectional spectrum, may lead to a consistent value of the total mss, $s^2 = s_x^2 + s_y^2$. We recall that this last quantity can be derived from the second moment of the omnidirectional spectrum:

$$s^2 = \int_0^\infty k^2 \Psi_0(k) dk. \tag{43}$$

We found that the wind speed dependence of the actual current can be very well fitted by a linear relation $u_c = 1.76\times$ windspeed -2.00 (in cm/s).

To validate the dispersion relation, a rough estimate of an averaged phase speed in the alongwind (c_x) direction as well as the averaged omnidirectional phase speed (c) was obtained by using the frequency elevation and slope spectra as follows:

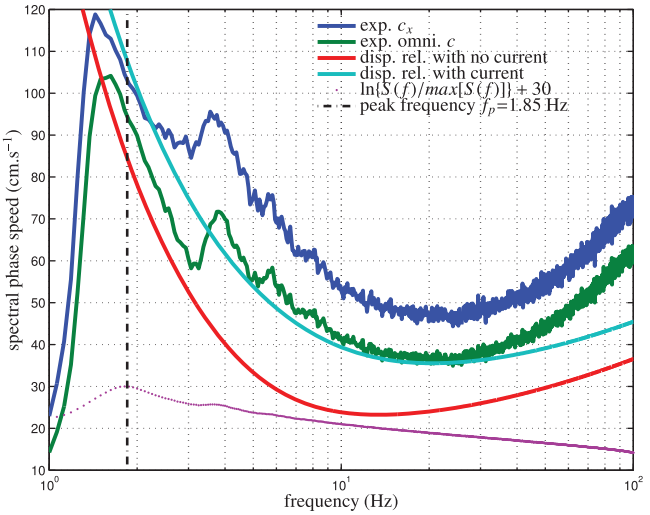

Figure 7. Experimental versus theoretical dispersion relation at wind speed 8 m/s. The renormalized frequency spectrum is shown for reference.

$$c_x^2(f) \simeq \frac{\omega^2 S(f)}{S_{\parallel}(f)},\ c^2(f) \simeq \frac{\omega^2 S(f)}{S_{\parallel}(f) + S_{\perp}(f)}. \tag{44}$$

Figure 7 shows a comparison between the theoretical current-corrected phase speed based on the linear dispersion relation and the corresponding experimental estimate at the highest wind speed when the current effect is the largest. We can see that the introduction of the current (adjusted a posteriori with the mss) make the dispersion relation in reasonable agreement with the omnidirectional phase speed in particular for the dominant peak and in the frequency range associated with the capillary-gravity waves generated by

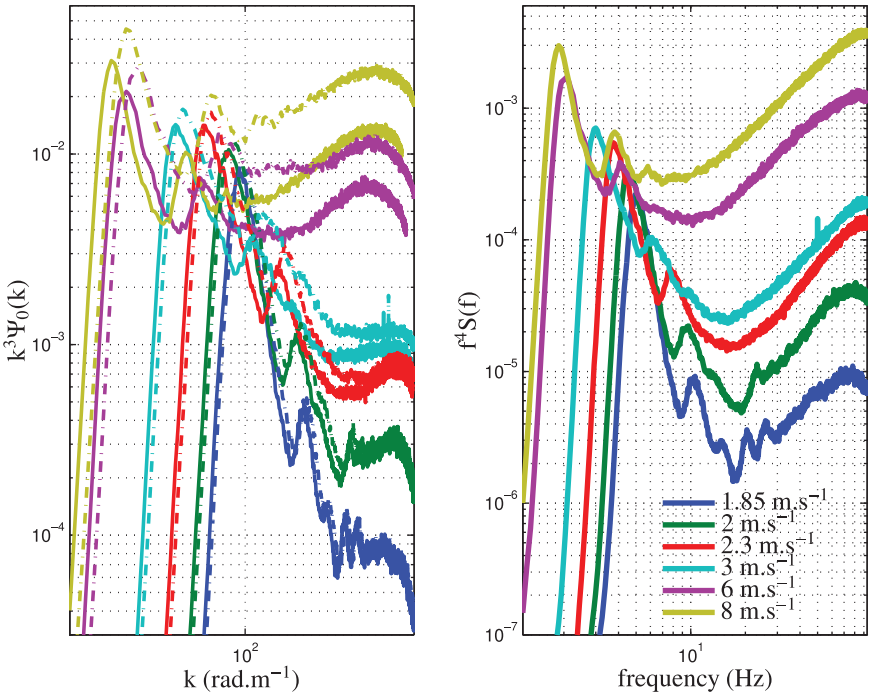

Figure 8. Omnidirectional wave number curvature spectra ($k^3\Psi_0(k)$) estimated for different wind speeds with (solid lines) and without (dashed lines) account of the surface current.

wind and propagating freely at the surface of dominant waves. In the frequency range around 5 Hz and above 50 Hz, the wavefield is composed of free and bound harmonics making both the theoretical and experimental celerity estimates less accurate or even significant.

To summarize, the omnidirectional spectrum is obtained from the experimental frequency spectrum via equation (39) and u_c while the spreading function (28) is estimated from $\alpha(k)$ using equation (36). Figure 8 shows the resulting omnidirectional curvature spectra at different wind speeds. We have superimposed on the same plot the omnidirectional spectra ($k^3\Psi_0(k)$) which would have been obtained if the surface current had been discarded (that is with $u_c = 0$ in the previous derivation). As seen, the current has an important effect at the highest wind speeds, with a downshift of the peak wave number and a significant reduction (roughly by a factor 2) of the level of curvature in the high-frequency part. Figure 9 shows the evolution of the parameter $\alpha(k)$ with wave number and Figure 10 shows the angular spreading function $Y(\phi)$ given by equation (36) for a few typical values of the parameter α. The behavior of the spreading function mirrors the contrast function $D(f)$ which was discussed earlier.

To assess the obtained wave number spectra it is important to perform a number of consistency tests. The most elementary test is the a posteriori verification of the integral constraints satisfied by the wave number spectrum. The significant wave height (H_s) can be calculated by integration of either the frequency or the omnidirectional wave number spectrum. As expected, the comparison of the respective values of H_s obtained in both ways show very consistent results. On the other hand, the along-(s_x^2) and across-wind mss (s_y^2) are related to the wave number spectrum by:

$$s_x^2 = \int_0^\infty dk\, k^2 \Psi_0(k) \int_0^{2\pi} Y(k,\phi) \cos^2\phi \, d\phi$$
$$s_y^2 = \int_0^\infty dk\, k^2 \Psi_0(k) \int_0^{2\pi} Y(k,\phi) \sin^2\phi \, d\phi. \quad (45)$$

These slope variances have been recalculated with the empirical wave number spectra and found in excellent agreement with the experimental values obtained from the integration of the slope spectra (20). The

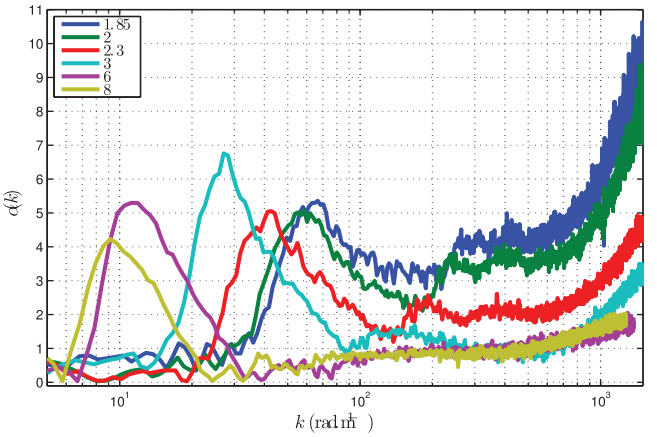

Figure 9. Variation with wind speed of the parameter α characterizing the spreading function $Y(k,\phi)$ given by equation (28) for different wind speeds.

relative differences are less than about 0.5% for the significant height H_s and 1% (respectively 7%) for the directional mss at the small (respectively large) wind speeds.

6. Scattering Model

6.1. Physical Optics Model

The interaction of electromagnetic waves with the sea surface in the microwave regime is a complex mechanism which has been the subject of an important amount of works in the literature. Starting with the asymptotic methods such as Bragg theory and the geometrical optics approximation (GO) which have a limited domain of validity, many unified models have been developed to obtain more robust approximations. We refer to, e.g., *Elfouhaily and Guérin* [2004] for a recent review on the analytical models and their respective merits. One of the most popular models in ocean remote sensing is the composite or two-scale model, according to which the scattering process is pictured by resonant scattering from ripples propagating on tilted rough facets of longer waves. In the context of describing the water surface microwave cross section in a wind-wave tank this model brings significant improvement over the Bragg theory at intermediate incidence [*Keller et al*., 1995; *Plant et al*., 1999]. However, at small incidence angles (θ) where polarization effects are negligible, it is well known that the simple Physical Optics approximation (PO) is sufficient for an accurate description of the NRCS and has been therefore adopted here. In its statistical formulation, that is assuming stationary surface statistics both in space and time, the PO monostatic NRCS is given by the so-called "Kirchhoff integral":

$$\sigma^0_{PO}=\frac{1}{\pi}\frac{K^2}{\cos^2\theta}|R|^2\int d\mathbf{r}\,\mathrm{e}^{-i\mathbf{Q_H}\cdot\mathbf{r}}\left(\mathrm{e}^{-\frac{Q_z^2}{2}S_2(\mathbf{r})}-\mathrm{e}^{-Q_z^2\rho(\theta)}\right), \tag{46}$$

where R is the Fresnel reflection coefficient on a flat water surface at normal incidence, $\mathbf{Q_H}$ and Q_z are the horizontal and vertical components of the Ewald vector $\mathbf{Q}=-2\mathbf{K}$, respectively, $\mathbf{K}$ is the incident wave vector and $K=2\pi/\lambda_{EM}$ the electromagnetic wave number. The integration is performed over the horizontal space vector $\boldsymbol{r}$ and the quantity S_2 is the structure function of elevation (6). The numerical evaluation of PO involves the computation of the auto-correlation function (ρ) and its integration into the Kirchhoff integral, a task which is in general made difficult by the oscillating and slowly decaying nature of the former.

The autocorrelation function (7) is obtained through the two-dimensional inverse Fourier transform of the wave number spectrum. To accelerate its systematic computation we first calculate the coefficients $\Delta_{2n}(k)$ of the Fourier azimuthal expansion (25) for the spreading function (28):

$$\begin{aligned}\Delta_0(k)&=1,\\ \Delta_{2p}(k)&=\frac{2}{\pi}\int_0^\pi d\varphi\cos(2p\,\varphi)Y(k,\varphi),\ p=1,2,\cdots.\end{aligned} \tag{47}$$

This provides readily an azimuthal expansion for the autocorrelation function into even harmonics:

$$\rho(r,\phi_r)=\rho_0(r)+\rho_2(r)\cos(2\phi_r)+\rho_4(r)\cos(4\phi_r)+\ldots \tag{48}$$

with:

$$\rho_{2p}(r)=(-1)^p 2\pi\int_0^\infty dk\,\Delta_{2p}(k)\Psi_0(k)J_{2p}(kr),\ p\geq 1, \tag{49}$$

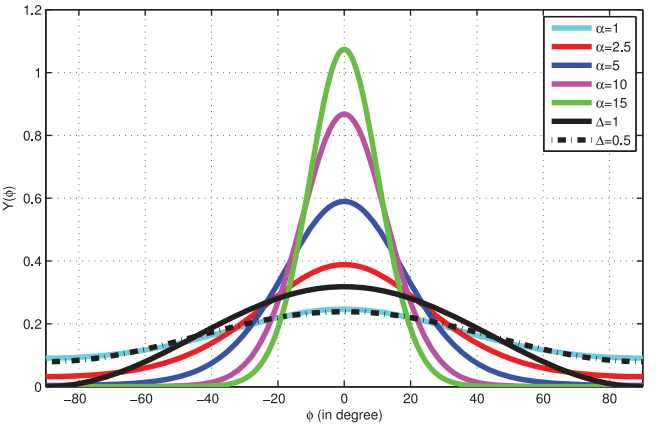

Figure 10. Angular spreading function $Y(\phi)$ given by equation (36) for a few typical values of α and comparison with Elfouhaily spreading function (26) for $\Delta=0.5$ and $\Delta=1$.

where J_{2p} is the first-kind Bessel function of order $2p$. We found that four harmonics ($p=1$–4) are sufficient to ensure a relative error less than 1% on the computation of the autocorrelation function. The calculation of the Kirchhoff integral has been carried out with a double integration in polar coordinates using Simpson integration rule. For isotropic or biharmonic spectra such as Elfouhaily spectrum it is customary to reduce this calculation to a single integral using Bessel transforms but this is not applicable here.

6.2. Geometrical Optics and Improved Version

In the limit of very large Rayleigh parameters ($Q_z^2\rho(\boldsymbol{\theta})\rightarrow\infty$), the PO reduces to the GO approximation, which is parameterized by the directional slopes only:

$$\sigma^0_{GO}=\frac{|R|^2}{2s_xs_y\cos^4\theta}\exp\left(-\frac{\tan^2\theta}{2}\left(\frac{\cos^2\phi}{s_x^2}+\frac{\sin^2\phi}{s_y^2}\right)\right), \tag{50}$$

where ϕ is the angle between the incidence wave vector and the wind direction. In the isotropic case ($s_x^2=s_x^2=s^2/2$) it simplifies further to:

$$\sigma^0_{GO}=\frac{|R|^2}{s^2\cos^4\theta}\exp\left(-\frac{\tan^2\theta}{s^2}\right). \tag{51}$$

The GO model has the considerable advantage of expediting the calculations and not involving the wave number spectrum other than through the mss. However, it has a narrow domain of validity as it is in principle only valid in the optical limit. To improve the GO model at finite wavelength, it is classically resorted [*Brown*, 1978] to a "radar mss," that is, a mss filtered at the radar wavelength. This approach was recently revisited with the GO4 model (O. Boisot et al., The GO4 model in near-nadir microwave scattering from the sea surface, submitted to *IEEE Transactions on Geoscience and Remote Sensing*, 2015) where it was shown that the GO model can be significantly improved with the introduction of an extra wavelength-dependent curvature parameter, referred to as effective mean square curvature (msc). In its isotropic version (considered here for simplicity), it is given by:

$$\sigma^0_{GO4}=\sigma^0_{GO}\times\left(1+\frac{\mathrm{msc}}{16K^2s^2\cos^2\theta}\left(2-4\frac{\tan^2\theta}{s^2}+\frac{\tan^4\theta}{s^4}\right)\right). \tag{52}$$

It is important to note that the slope parameter s^2 entering into the GO4 model is the total and not the filtered mss. The curvature parameter msc was shown in O. Boisot et al. (submitted manuscript, 2015) to be approximately the cumulated spectral curvature ($k^4\Psi(k)$) with a cutoff at the EM wave number K. The total mss and the curvature parameter msc can be estimated jointly from the measurement of the NRCS at several incidences even in the absence of absolute calibration.

6.3. Non-Gaussian Corrections

Several recent works [e.g., *Mouche et al.*, 2007; *Bringer et al.*, 2012] have shown the importance of non-Gaussian corrections in the fine simulation of the backscattering cross section from the sea surface. They contribute to a slight increase of NRCS at nadir (peakedness correction) and separate the upwind and downwind directions (skewness correction). However, non-Gaussian corrections are based on cumulant expansions in the Kirchhoff integral, whose applicability for wind tank wave fields is not granted. Furthermore, they require the knowledge of higher-order structure functions, for which only coarse estimates are

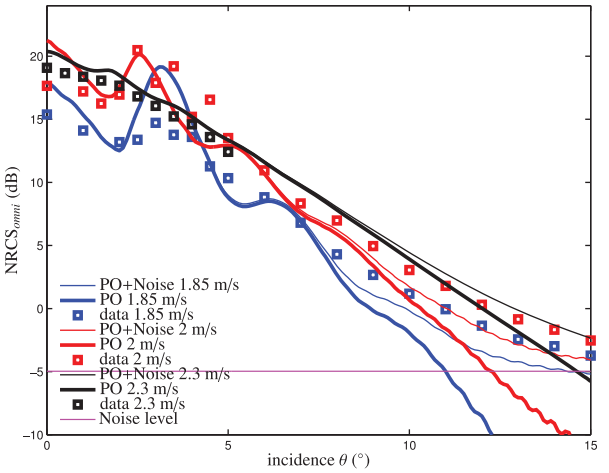

Figure 11. Experimental (data) omnidirectional NRCS for small wind speed and comparison with the PO model (PO) with and without noise.

available [*Caulliez and Guérin*, 2012; *Mironov et al.*, 2012]. Given these uncertainties and given the small amplitude of the expected correction we decided to limit ourselves to the classical Gaussian model.

7. Experimental Observations and Model Assessment

The full backscattering model developed here both concerns the empirical retrieval of the wave field directional wave number spectrum (section 5) and its incorporation in the PO model. The value of the freshwater complex permittivity in Ka band, which enters in the Fresnel reflection coefficient, has been set to $\varepsilon = 21.73 + i30.28$ according to the model by *Meissner and Wentz* [2004]. Note that it is very close to its seawater value $\varepsilon = 19.97 + i30.02$, therefore allowing direct comparison with in situ data.

To compare the simulated backscattering values with the related observations described above, it is necessary to correct the experimental values by the appropriate offset for retrieving the absolute levels of NRCS. Even though the radar system has been carefully calibrated, we can double-check the calibration coefficient by deriving them again by means of an indirect procedure. The offset was chosen by minimizing the least square error between the experimental and simulated NRCS in the upwind and downwind directions within the 5° of incidence around nadir at the three largest wind speeds. The low wind speeds have not been used in such a calibration test owing to the strongly oscillating nature of the scattering diagram at small incidences. We found at posteriori that the recalculated offset is 0.7 dB higher than the experimentally measured calibration coefficient, for which we have an uncertainty of ± 1.4 dB. This procedure thus cross-validates the model and the calibration technique. At the same time, it provides an estimate of the accuracy of the absolute levels of NRCS which are evaluated experimentally and numerically in this paper. The noise level could be estimated by using the radar echo on the water surface at rest (no wind). It was approximately rated to -5 dB after calibration. A part of the noise is of thermal origin. Another part may come from an imperfect damping of the spurious multiples reflections from the walls and the metallic parts of the experimental setup which could not be completely covered with radar absorbers. At last, an indirect source of error is the fact that radar measurements were averaged over not long-enough time series, in particular at high winds. Note that the parasitic reflections from the walls is likely to be higher in the crosswind direction at large incidences as in such a configuration, the incident beam undergoes the largest excursion from the center of the water tank toward the tunnel sidewalls. In view of their general behavior which leads to draw distinct inferences, the measurements have been classified into two families, respectively, referring to small wind and to large wind speed conditions. For a given wind speed, the experimental omnidirectional NRCS have been estimated by averaging the measurements made at one incidence in the various azimuthal planes investigated, that is $\phi_K = 0, 45, 90, 135,$ 180 degrees. The simulated omnidirectional NRCS has been defined in the same way as the observed NRCS.

7.1. Small Wind Speeds

Figure 11 displays the omnidirectional NRCS observed at various incidences for 1.85, 2, and 2.3 m/s wind speeds. Superimposed in thick lines are the omnidirectional NRCS predicted by the PO model (referred to as "PO") using the experimentally devised wave number spectra. To evaluate the effect of the noise we added a constant value of -5 dB to the modeled NRCS. In the figure, this noise level is marked by a thin line. An excellent agreement is found with the data. The most striking

Table 2. Modeled (m) and Observed (o) Angular Position and Angular Width of the NRCS Peak (in Degree) for the Smallest Two Wind Speeds (Given in m/s)

Wind Speed	k_p (rad/m)	θ_b (m)	θ_b (o)	$\Delta\theta_b$ (m)	$\Delta\theta_b$ (o)
1.85	98.21	3.58	3.5	1.5	1.7
2	74.76	2.72	2.75	1.3	1.8

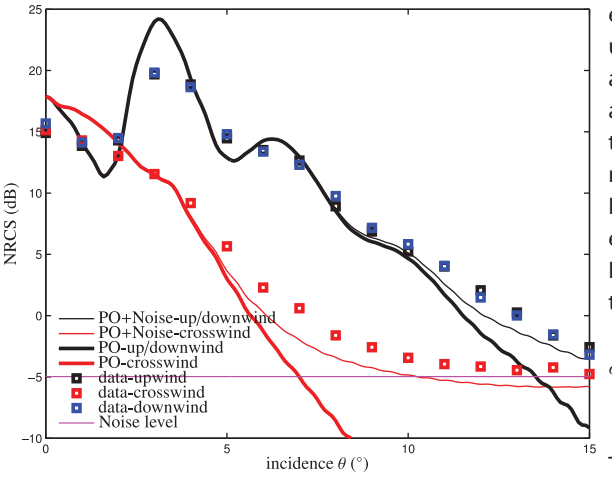

Figure 12. Experimental (data) directional NRCS for a 1.85 m/s wind speed at different azimuths and corresponding values calculated by the PO model (PO) with and without noise.

experimental fact is the occurrence of an unusual off-nadir maximum at an angle of about 3°. This phenomena can be very well accounted for by the Bragg theory as well as the PO model when applied to small roughness (both theories agreeing at small angles). In fact, when assumed a small Rayleigh parameter ($Q_z^2\rho_0 \ll 1$), the exponential term in the Kirchhoff integral (46) can be approximated by the first terms of the corresponding series:

$$\sigma^0_{PO}=\frac{1}{\pi}\frac{K^2}{\cos^2\theta}|R|^2\int d\boldsymbol{r}\,\mathrm{e}^{-i\boldsymbol{Q_H}\cdot\boldsymbol{r}}\left(Q_z^2\rho+\frac{1}{2}(Q_z^4\rho^2)+\ldots\right). \tag{53}$$

The leading term is proportional to the Fourier Transform of the autocorrelation function, namely the two-dimensional wave number spectrum Ψ, evaluated at wave vector $\boldsymbol{k}=\boldsymbol{Q}_H$. This term reaches its maximum at the incidence angle θ_b for which the Bragg wave number $Q_H=2K\sin\theta_b$ coincides with the surface wave spectral peak wave number (k_p):

$$\theta_b=\arcsin\left(\frac{k_p}{2K}\right). \tag{54}$$

The full width at half-maximum (FWHM) of the NRCS peak can also be predicted from physical considerations. From the gravity wave dispersion relationship (neglecting the impact of current at such small wind speeds as well as the effect of surface tension on the estimation of the peak wave number) we can also derive a relationship between the FWHM of the peak of the frequency spectra and the corresponding one of the wave number spectra, as follows:

$$\Delta k_p=\frac{8\pi^2}{9.81}f_p\Delta f_p. \tag{55}$$

With the resonant angle condition (54), we can express the corresponding FWHM in incidence angle, thus providing an order of magnitude of the width of the NRCS peak observed around the Bragg angle. This results in the following estimation for the angular width:

$$\Delta\theta_b \simeq \frac{\Delta k_p}{2K}. \tag{56}$$

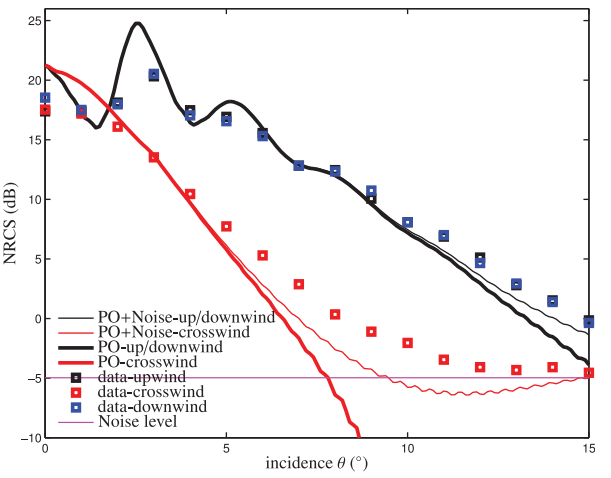

Figure 13. Same as Figure 12 for a 2 m/s wind speed.

The values of the observed peak wave number (k_p), the observed and predicted angular position (θ_b) as well as the FWHM ($\Delta\theta_b$) of the maximum NRCS at the smallest two wind speeds are reported in Table 2. The values observed at the largest wind speed (2.3 m/s) have been discarded because the peak in that case is not sufficiently marked. An excellent agreement is observed between the actual and predicted values.

Figures 12 and 13 show the directional NRCS in selected azimuthal planes, namely along the upwind ($\phi=0^\circ$), downwind ($\phi=180^\circ$), and crosswind ($\phi=90^\circ$) directions at small wind speeds (the 2.3 m/s data set is incomplete and is not shown).

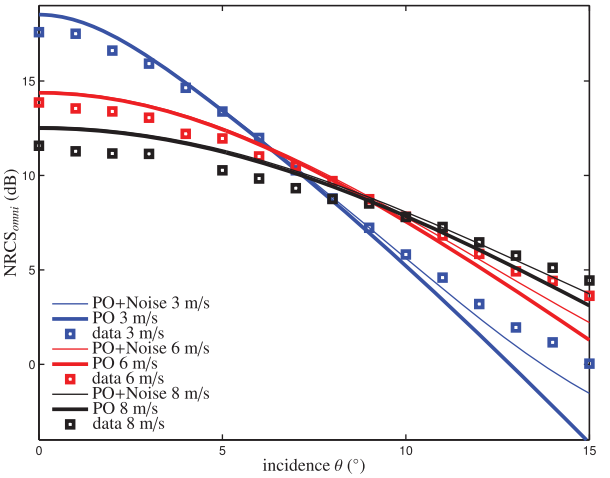

Figure 14. Experimental (data) omnidirectional NRCS for medium and large wind speed and comparison with the PO model (PO) with and without noise.

The weaker return in the crosswind direction is corrupted by the noise level beyond 6–7° of incidence. The most notable feature is a marked upwind-crosswind contrast, which can be as high as 10 dB. The observed upwind-downwind asymmetry is less than about 0.5 dB and therefore not significant as it is smaller than the expected accuracy of the experimental data. The peak of NRCS at small incidences attributed to the Bragg mechanism is not seen in the crosswind direction. This is linked to the absence of resonant Bragg waves in the crosswind direction, the typical size of the rhombic patterns corresponding to a too small wave number compared to the resolution in incidence angle and the random nature of the patterns being more pronounced in this direction due to the inhomogeneity of wave fields generated at such low winds. Note that the absence of a NRCS bump in the crosswind direction excludes the possibility that the latter could be generated by a spurious effect induced by the radar antenna configuration, in particular the radar sidelobes. Note as well that the NRCS bump, decreasing in amplitude, is visible up to an azimuthal angle of 45° on both sides of the wind direction. Altogether the model is found in good agreement with the data in the angular domain of interest, namely the first degrees of incidence.

Another striking feature of the NRCS observed at low winds is the unusual wind speed dependence of its nadir value, which is seen to increase with this parameter. This is opposite to what is generally observed in open sea with altimeters. However, this peculiarity might be ascribed to the increase of the intermittent behavior of the wave field at such light winds, the wave growth occurring primarily inside well-distinguishable wave patches at the water surface visualized in time records by the presence of well-pronounced wave groups. Consistently, this behavior induces an increase in the incoherent part of the radar return at nadir.

7.2. Large Wind Speeds

Figure 14 displays the omnidirectional NRCS at 3, 6, and 8 m/s wind speed. The PO model is found very accurate in the first 10° of incidence and, once corrected with noise, remains within 1 dB from the experimental values over the whole range of incidences. A minimum of sensitivity of the NRCS to wind speed is observed around the incidence angles of 7−8°, where the corresponding three scattering diagrams almost intersect.

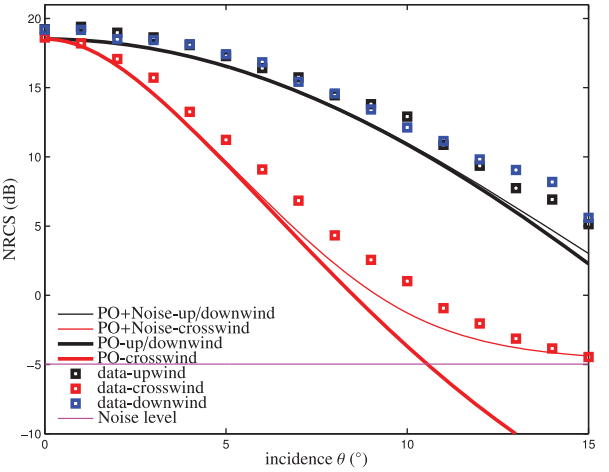

Figure 15. Same as Figure 12 for 3 m/s wind speed.

Figures 15–17 show the directional NRCS in the upwind, downwind and crosswind directions for increasing wind speeds. One can notice an increasing separation of the upwind and crosswind return with incidence, which is reasonably well reproduced by the model after noise correction. The observed upwind/crosswind asymmetry can be as high as 10 dB at 15° incidence. It is much stronger than that observed at sea which is of the order of 2 dB only [see, e.g., *Tanelli et al.*, 2006, Figure 3]. At the largest wind speeds, the model

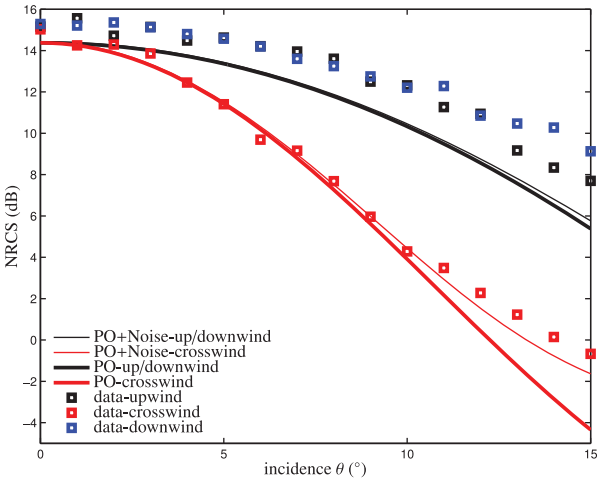

Figure 16. Same as Figure 12 for 6 m/s wind speed.

underestimates the NRCS in the upwind/downwind direction by about 1 dB. This is likely to be due to the increasing contribution of non-Gaussian features of the water surface (in particular the peakedness which has not been taken into account here). Note also that the downwind return at the largest incidence and wind speed seems to be slightly larger than the upwind counterpart whereas it is the contrary which is in general observed in open sea. A confirmation of this phenomenon would, however, require a better accuracy in the NRCS measurements (for example by performing longer time series) and is left for further investigation. Note that the observed discrepancy at nadir (±0.5 dB variation) is also caused by insufficient convergence of the time series. As was discussed in section 3.2, the averaging process is indeed more demanding in time for large wind speeds since it requires a certain number of dominant waves to pass into the illuminated surface patch.

8. Comparison With GO and GO4 Models

For practical applications where the roughness spectrum is unknown it is useful to have a simple scattering model at hand with a limited number of parameters. To this aim we tested the GO model and its improvement GO4 for the highest wind speed cases and for the omnidirectional NRCS. Note that the GO and GO4 models are bound to fail at smallest wind speed where they are not capable to reproduce the nonmonotonic behavior of the NRCS with the incidence angle. We calculated the GO model with the filtered mss at $K/3$, that is, from the integration of the wave number spectrum to this cutoff value. For the GO4 model we did not use any a priori knowledge on the surface (this is the strength of the model) but made a joint estimation of the mss and msc parameters with a least square fitting of the scattering data over the available range of incidence (see O. Boisot, submitted manuscript, 2015 for details of the technique). We obtained the values (1.56, 3.13, and 4.51%), respectively, for the total mss at wind speed 3, 6, and 8 m/s, in close agreement with the experimentally observed values of this parameter. The corresponding values of the effective msc were found to be 444, 1025, and 1490 m^{-2}. These values of the msc are consistent with the wave spectrum model as they correspond to a partial fourth moment of the experimental wave number spectrum at a cutoff value close to the EM wave number K and provides an additional validation test of the short-wave spectrum model. As seen in Figure 18, the GO4 brings a significant improvement over the regular GO model and remains accurate over the whole set of incidence. Note that it can even bring a significant improvement over the PO model, as seen at 3 m/s wind speed. They are essentially two reasons for this result which might be surprising at first sight. First, the GO4 parameters are estimated directly from the experimental radar data and do not require the a priori determination of the wave number spectrum whose estimation can suffer from inaccuracies.

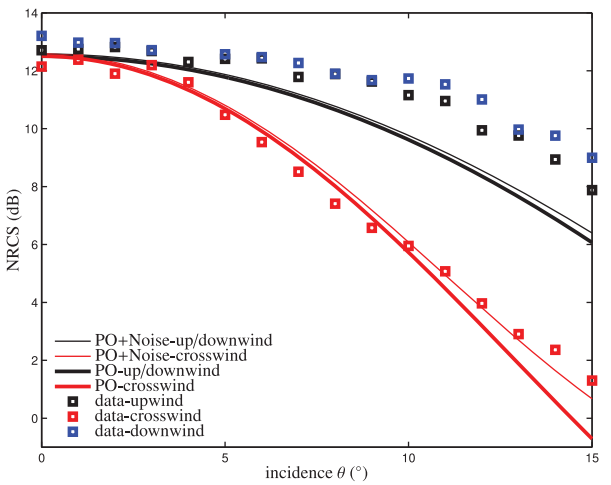

Figure 17. Same as Figure 12 for 8 m/s wind speed.

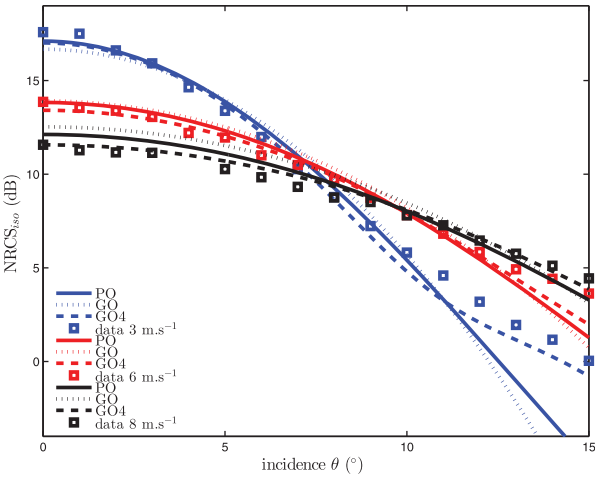

Figure 18. Experimental (data) omnidirectional NRCS for medium and large wind speeds and comparison with the PO, the GO, and GO4 models.

Second, as shown in O. Boisot (submitted manuscript, 2015), the GO4 automatically incorporates in the msc parameter an important non-Gaussian feature of the surface, namely the excess kurtosis coefficient of the slope distribution, which cannot be rendered easily with the PO and may have a nonnegligible contribution to the scattering diagram at low incidence (it is actually at 3 m/s wind speed that the excess kurtosis of slope was found to be the strongest). However, the GO4 is an asymptotic theory which requires large Rayleigh parameter. It can therefore not replace the PO at the lowest wind speeds where the surface roughness is small.

9. Comparison With In Situ Data

In view of future applications of the Ka-band to the characterization of the ocean surface or continental waters it is important to evaluate in which respect our findings are representative of natural surfaces.

9.1. Comparison With Oceanic Surfaces

Besides the obvious effect of fetch which makes wind waves generated in a tank and open sea surfaces very different, one might wonder whether the small-scale components (which are the resonant scatterers in Ka-band) differ from those predicted by unified wave number spectra. We have therefore performed a comparison with the reference spectra proposed by *Elfouhaily et al.* [1997] and *Kudryavtsev et al.* [2003a, 2003b] at short fetches, which we refer to by the name of their first author. Figure 19 shows the experimental wave number spectra estimated at two wind speeds plotted together with the Elfouhaily and Kudryavstev wave number curvature spectra evaluated at same winds. The input parameters of these models have been adjusted to make the comparison meaningful, i.e., the wave age parameter Ω or the fetch X have been fixed to match the peak wave number and the wind-wave tank wind speed (U) has been converted into a wind speed at 10 m above the surface (U_{10}) through the empirical relationship observed at large fetches in the wind tunnel [*Caulliez et al.*, 2008]:

$$U_{10} = 1.28U - 0.63. \tag{57}$$

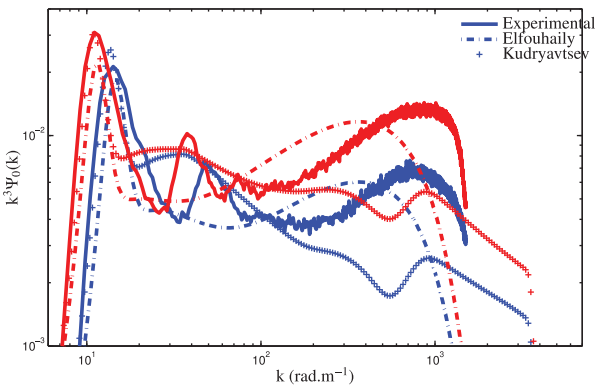

Figure 19. Comparison of the experimentally derived curvature spectrum (solid lines) with Elfouhaily (dashed dotted lines) and Kudryavtsev (symbols) spectral models. The blue lines correspond to a 6 m/s wind speed (U_{10} = 7.05 m/s) and the red lines to a 8 m/s wind speed (U_{10} = 9.61 m/s).

For the Elfouhaily spectrum we obtain the values Ω=8.5 and Ω=10.3 for the wave age defined as the ratio between the dominant phase speed and U_{10}. These values are close to those (Ω=10.1 and Ω=12.2, respectively) predicted by the fetch-wave age relationship given by *Elfouhaily et al.* [1997] (equation (37)) for a fetch of 28 m. For the Kudryavstev spectrum the matching of the spectral peak is obtained for a fetch X = 100 m, that is larger than the actual value (28 m) but of the same order of

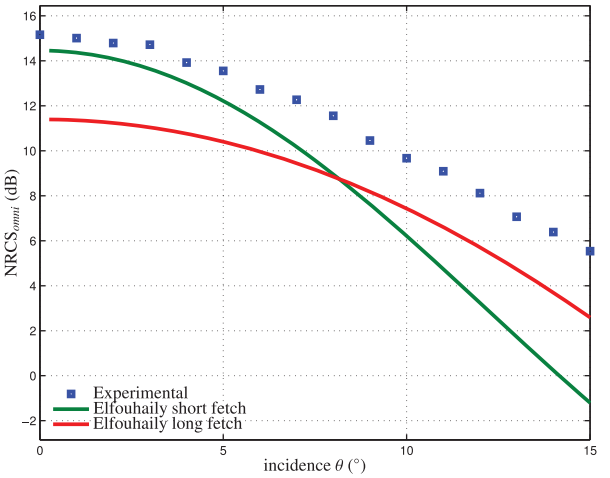

Figure 20. Omnidirectional NRCS according to the experimental wind-wave tank spectrum and Elfouhaily unified model at infinite and short fetch, by a common wind $U_{10} = 7.05$ m/s.

magnitude. As seen in Figure 19, the experimental spectra are found intermediate between the two spectral models. The level of the curvature spectrum predicted by Elfouhaily model is closer to our experimental findings with, however, a shift in the position of the short-wave range curvature peak. The position of this peak is found consistent with Kudryavstev model which, in turn, underestimates its amplitude. As to the difference in the high-frequency decay ($k > 1000$ rad/m), it is due to the effect of the instrumental filtering in the instantaneous wave signals and is not physically relevant. The difference in the wave number spectra results in significant discrepancy in the near-nadir NRCS, as shown in Figure 20.

To compare the directionality derived from the experimental wave number spectra with that considered by Elfouhaily model, we evaluated the upwind-downwind ratio (26) which in the present case is given by:

$$\Delta(k) = \tanh(\alpha_k/2). \tag{58}$$

Figure 21 shows the upwind/crosswind ratio derived from wave slope measurements at high winds plotted in comparison with the parametric function proposed by *Elfouhaily et al.* [1997] for the same wind and wave age conditions as these considered above for the omnidirectional spectra. An important difference is seen at the lowest frequencies where the actual $\Delta(k)$ function reaches its maximum value 1 only in the vicinity of the spectral peak wave number, contrarily to the Elfouhaily model which simply assumes a plateau at this maximum value. The level of the upwind/crosswind ratio is found consistent with Elfouhaily model at intermediate frequencies but takes higher values at the highest frequencies, a fact which may account for the directional effect of wind on small-scale wave energy supply.

There are very few available data in the literature reporting detailed measurements of NRCS at different incidences in Ka band. In the airborne campaign described in *Tanelli et al.* [2006], Ku and Ka-band airborne measurements were collected in a wide range of incidence angle away from nadir. The flights were carried out over Wakasa Bay in Japan. Even through the description of the corresponding sea state and wind speed is very coarse, it helps making an overall qualitative comparison with the NRCS measured in laboratory. A large number of approximate wind speeds and directions were reported in this experiment for the different run days. We have reproduced in Figure 22 the extremal values (Figure 1d) of *Tanelli et al.* [2006] corresponding to the lowest and highest (>20 m/s) wind speeds, as well as intermediate values (8–12 m/s). Superimposed are the omnidirectional NRCS observed in the wind-wave tank at 3 and 8 m/s wind speeds. At small wind speed, airborne and laboratory NRCS show

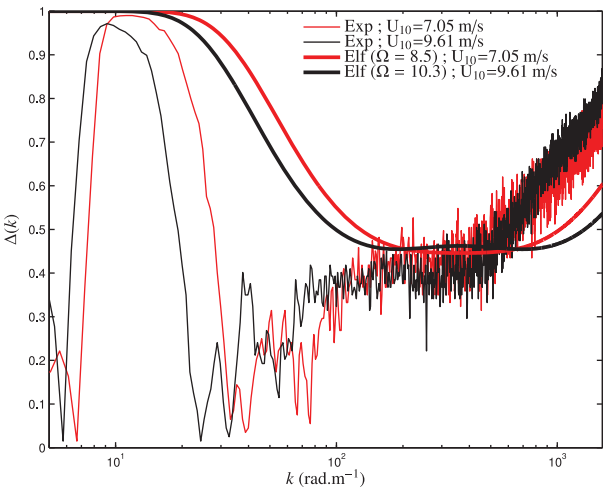

Figure 21. Upwind-downwind ratio $\Delta(k)$ derived from the experimental (thin lines) wave slope spectra and the Elfouhaily spreading functions (thick lines) at 6 m/s wind speed ($U_{10} = 7.05$ m/s, red lines) and 8 m/s wind speed ($U_{10} = 9.61$ m/s, black lines).

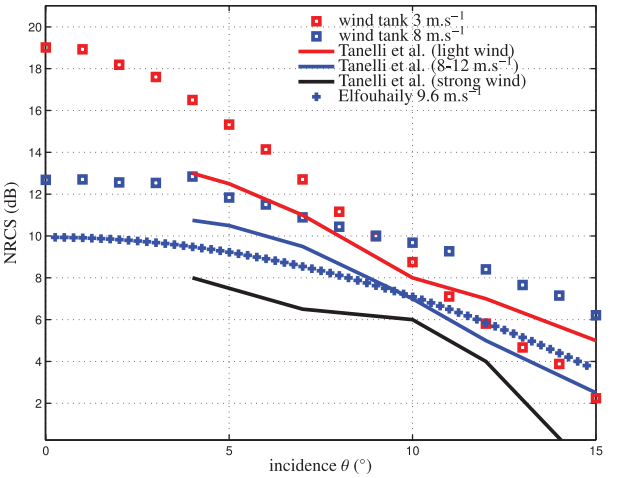

Figure 22. Comparison of NRCS with oceanic surfaces.

very different levels of NRCS (about 4 dB at 4° incidence and even more if one extrapolate the plot to nadir). A better agreement is reached at moderate wind speed ($U10=8-12$ m/s for airborne data, $U10=9.6$ m/s for wave tank), where the discrepancy is reduced to about 2 dB. The simulated NRCS with a fully developed omnidirectional Elfouhaily spectrum is shown for reference. It is slightly lower, which can be explained by the fact that the sea state in Wakasa Bay is in fetch-limited conditions, but quite consistent in shape. This seems to indicate that the order of magnitude of the NRCS observed in laboratory for the highest wind speed are close to those from fetch-limited seas but differs largely at low wind speed.

9.2. Comparison With Continental Water Surfaces

A comparison with continental water surfaces was made using the airborne DRIVE-BUSARD campaign described in *Fjortoft et al.* [2014]. The aircraft was equipped with a Ka-band SAR instrument developed by ONERA (DEMR Salon de Provence) and adapted for working at low incidence. The data were calibrated using corner reflectors on the ground. Several flights were conducted over the Rhone river, the Vaccares lake and the Mediterranean shore by a very calm day, where the wind speed was estimated around 3–4 m/s. Figure 23 shows the recorded NRCS as a function of the incidence angle and a comparison with the omnidirectional wind-wave tank values at 2 and 3 m/s wind speed. An excellent agreement is found with the airborne measurements over the Rhone river and the laboratory measurement by 2 m/s wind speed. Note that the strong current in the Rhone river (about 1.5 m/s in the region of Arles) must be taken into account in comparing the wind speed as it reduces significantly the relative speed of the airflow at the water surface. The simulated NRCS for a fully developed Elfouhaily spectrum is given for reference at 3 m/s wind speed and is seen to be dramatically different at low incidence. This confirms the aforementioned statement that oceanic surfaces observed at small wind speed are very different.

10. Conclusions

Observations in a large wind-wave tank and modeling of Ka-band radar scattering from the water surface were combined to investigate in more details the electromagnetic response of oceans and lakes in this high-frequency microwave range. On the grounds of physical models and well-controlled experiments, we have proposed a proper description of the statistical properties of water surface roughness at small scales and the radar backscatter. Using fine wave height and slope measurements, we have developed an empirical wave number spectrum model addressing the gravity-capillary wave range and taking into account the water drift current. This model has been combined with the physical optics and the geometrical optics (GO and GO4) scattering model. Our study has unveiled unconventional behavior of the cross section for specific radar configuration and wind speed conditions. Our main results and conclusions can be summarized as follows:

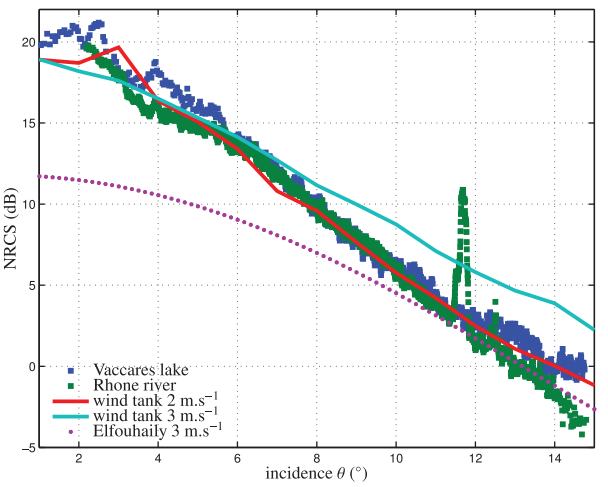

Figure 23. Comparison with continental water surfaces.

1. At large fetches and for moderate to large wind speeds, the frequency spectrum of the surface wave elevation observed in the laboratory can be reasonably well described by a JONSWAP shape around the peak frequency. The high-frequency tail, however, exhibits a more complicated, wind-dependent behavior which mirrors the change in nonlinear wave behavior with wave scale as wind speed is increased.
2. The derivation of the directional wave number spectrum from the frequency spectrum could be made by verifying that the Doppler-shift induced by long-wave orbital velocities is negligible and assuming only a constant drift current in the wave dispersion relationship. We found that the omnidirectional wave number spectrum is very sensitive to the magnitude of the drift current and can be inverted from the frequency spectrum under a number of simplifying assumptions. We have shown that the slope spectra derived from laser slope gauge measurements in the longitudinal and transverse directions are sufficient to parameterize the angular spreading function, when taken an Ansatz on its analytical form. The Elfouhaily biharmonic model is not relevant in the context of a wind tank experiment where contrasted directional slope ratio are observed and a more directive angular dependence of the two-dimensional wave number spectrum has been employed.
3. Observations and simulations have been systematically compared. Among the test cases, two families have been identified, namely experiments at small (1.85, 2, and 2.3 m/s) and at large (3, 6, and 8 m/s) wind speeds. At small wind speeds, a nonconventional behavior dependence of the nadir radar response on wind speed as well as a marked maximum around 3° in along-wind incidence were observed. This striking peculiarity can be explained and predicted by the well-known Bragg mechanism. At large incidences, a more classical wind dependence is observed, with a marked upwind-crosswind asymmetry. A minimum of sensitivity to wind speed is observed around 7°. The overall agreement between the results derived from the physical optics scattering model and the radar data is satisfactory while the classical GO model performs poorly even by the strongest wind speed. The recent GO4 model turns out to be accurate from moderate to large wind speeds (3–8 m/s) and the estimation of its slope and curvature parameters from the experimental NRCS is consistent with the obtained directional spectrum.
4. Qualitative comparisons have been performed with in situ measurements and models in oceanic as well as continental conditions. From the comparison with commonly used ocean wave spectrum models, it is found that fetch is not the only source of discrepancy in the wave number spectra. When compared with NRCS recorded over fetch-limited sea surface, very different levels and shapes are observed at small wind speed but comparable results are obtained at larger wind speed (8 m/s). At low wind speed, the wind-wave tank results are found consistent with values recorded over lakes and rivers.

These observations have shown that the study of near-nadir Ka-band scattering in a large wind-wave tank is already very rich and informative and can be compared to some extent to in situ conditions. This study must be depended to confirm the partial conclusions which were already drawn concerning the spatial properties of wind wave fields. In future experimental campaigns, we hope that some technical improvements will be achieved in the light of this first set of measurements (longer time series, increased radar dynamics to explore higher incidences, comparison with more established radar response in Ku-band, etc.).

Acknowledgments
This work was supported by CNES under research contracts R-S12/OT-0003–056 and DCT/SI/AR/2012–9643. Olivier Boisot is granted by CNES and CLS. We thank the technical staff from Pytheas and IRPHE for their assistance during the experiments. The data used in this study are available for verification purposes upon request to the corresponding author (guerin@univ-tln.fr).

References

Bringer, A., C.-A. Guérin, B. Chapron, and A. Mouche (2012), Peakedness effects in near-nadir radar observations of the sea surface, *IEEE Trans. Geosci. Remote Sens.*, *50*(9), 3293–3301.

Brown, G. S. (1978), Backscattering from a Gaussian-distributed perfectly conducting rough surface, *IEEE Trans. Antennas Propag.*, *26*(3), 472–482.

Caulliez, G., and F. Collard (1999), Three-dimensional evolution of the wind waves from gravity-capillary to short gravity range. European, *J. Mech. B/Fluids*, *18*(3), 389–402, doi:10.1029/2012JC008402.

Caulliez, G. (2013), Dissipation regimes for short wind waves, *J. Geophys. Res. Oceans*, *118*, 672–684, doi:10.1029/2012JC008402.

Caulliez, G., and C.-A. Guérin (2012), Higher-order statistical analysis of short wind-waves, *J. Geophys. Res.*, *117*, C06002, doi:10.1029/2011JC007854.

Caulliez, G., V. Makin, and V. Kudryavtsev (2008), Drag of the water surface at very short fetches: Observations and modeling, *J. Phys. Oceanogr.*, *38*(9), 2038–2055.

Coantic, M., and P. Bonmarin (1975), The air-sea interaction simulation facility at the Institut de Mécanique Statistique de la Turbulence, *Atmos. Technol.*, *7*, 72–79.

Durand, M., L. Fu, D. Lettenmaier, D. Alsdorf, E. Rodriguez, and D. Esteban-Fernandez (2010), The surface water and ocean topography mission: Observing terrestrial surface water and oceanic submesoscale eddies, *IEEE Proc.*, *98*(5), 766–779.

Dyer, F., M. Gary, and G. Ewell (1974), Radar sea clutter at 9.5, 16.5, 35, and 95 GHz, in *Antennas and Propagation Society International Symposium*, vol. 12, pp. 319–322, IEEE, Georgia Institute of Technology, Atlanta, Ga.

Elfouhaily, T., and C.-A. Guérin (2004), A critical survey of approximate scattering wave theories from random rough surfaces, *Waves Random Complex Media*, *14*(4), 1–40.
Elfouhaily, T., B. Chapron, K. Katsaros, and D. Vandemark (1997), A unified directional spectrum for long and short wind-driven waves, *J. Geophys. Res.*, *102*(C7), 15,781–15,796.
Ermakov, S., I. Kapustin, and I. Sergievskaya (2010), Tank study of radar backscattering from strongly nonlinear water waves, *Bull. Russ. Acad. Sci. Phys.*, *74*(12), 1695–1698.
Fjortoft, R., et al. (2014), KaRin on SWOT: Characteristics of near-nadir Ka-band interferometric SAR imagery, *IEEE Trans. Geosci. Remote Sens.*, *52*(4), 2172–2185.
Gade, M., W. Alpers, S. A. Ermakov, H. Hühnerfuss, and P. A. Lange (1998), Wind-wave tank measurements of bound and freely propagating short gravity-capillary waves, *J. Geophys. Res.*, *103*(C10), 21,697–21,709.
Giovanangeli, J.-P., L. F. Bliven, and O. Le Calve (1991), A wind-wave tank study of the azimuthal response of a Ka-band scatterometer, *IEEE Trans. Geosci. Remote Sens.*, *29*(1), 143–148.
Hara, T., E. J. Bock, and D. Lyzenga (1994), In situ measurements of capillary-gravity wave spectra using a scanning laser slope gauge and microwave radars, *J. Geophys. Res.*, *99*(C6), 12,593–12,602.
Hasselmann, K., et al. (1973), Measurements of wind-wave growth and swell decay during the joint north sea wave project (JONSWAP), *Dtsch. Hydrogr. Z*, *A8*(12), 1–95.
Hughes, B. (1978), The effect of internal waves on surface wind waves. 2: Theoretical analysis, *J. Geophys. Res.*, *83*(C1), 455–465.
Hwang, P. A. (2006), Doppler frequency shift in ocean wave measurements: Frequency downshift of a fixed spectral wave number component by advection of wave orbital velocity, *J. Geophys. Res.*, *111*, C06033, doi:10.1029/2005JC003072.
Hwang, P. A., D. M. Burrage, D. W. Wang, and J. C. Wesson (2013), Ocean surface roughness spectrum in high wind condition for microwave backscatter and emission computations, *J. Atmos. Oceanic Technol.*, *30*(9), 2168–2188.
Keller, M. R., B. L. Gotwols, W. J. Plant, and W. C. Keller (1995), Comparison of optically-derived spectral densities and microwave cross sections in a wind-wave tank, *J. Geophys. Res.*, *100*(C8), 16,163–16,178.
Kudryavtsev, V., D. Hauser, G. Caudal, and B. Chapron (2003a), A semiempirical model of the normalized radar cross-section of the sea surface. 1: Background model, *J. Geophys. Res.*, *108*(C3), 8054, doi:10.1029/2001JC001003.
Kudryavtsev, V., D. Hauser, G. Caudal, and B. Chapron (2003b), A semiempirical model of the normalized radar cross-section of the sea surface: 2. Radar modulation transfer function, *J. Geophys. Res*, *108*(C3), 8055, doi:10.1029/2001JC001004.
Long, M. (2001), *Radar Reflectivity of Land and Sea*, Artech House, Norwood, Mass.
Masuko, H., K. Okamoto, M. Shimada, and S. Niwa (1986), Measurement of microwave backscattering signatures of the ocean surface using X band and Ka band airborne scatterometers, *J. Geophys. Res.*, *91*(C11), 13,065–13,083.
Meissner, T., and F. J. Wentz (2004), The complex dielectric constant of pure and sea water from microwave satellite observations, *IEEE Trans. Geosci. Remote Sens.*, *42*(9), 1836–1849.
Mironov, A. S., M. V. Yurovskaya, V. A. Dulov, D. Hauser, and C.-A. Guérin (2012), Statistical characterization of short wind waves from stereo images of the sea surface, *J. Geophys. Res.*, *117*, C00J35, doi:10.1029/2011JC007860.
Mouche, A., B. Chapron, N. Reul, D. Hauser, and Y. Quilfen (2007), Importance of the sea surface curvature to interpret the normalized radar cross section, *J. Geophys. Res.*, *112*, C10002, doi:10.1029/2006JC004010.
Nekrasov, A., and P. Hoogeboom (2005), A Ka-band backscatter model function and an algorithm for measurement of the wind vector over the sea surface, *IEEE Geosci. Remote Sens. Lett.*, *2*(1), 23–27, doi:10.1109/LGRS.2004.840613.
Phillips, O. (1977), *The Dynamics of the Upper Ocean*, Cambridge Univ. Press, U. K.
Plant, W. J. (2015), Short wind waves on the ocean: Wavenumber-frequency spectra, *J. Geophys. Res. Oceans*, *120*, 2147–2158, doi:10.1002/2014JC010586.
Plant, W. J., W. C. Keller, V. Hesany, T. Hara, E. Bock, and M. A. Donelan (1999), Bound waves and Bragg scattering in a wind-wave tank, *J. Geophys. Res.*, *104*(C2), 3243–3263.
Plant, W. J., P. H. Dahl, J.-P. Giovanangeli, and H. Branger (2004), Bound and free surface waves in a large wind-wave tank, *J. Geophys. Res.*, *109*, C10002, doi:10.1029/2004JC002342.
Smirnov, A. V., I. M. Fuks, and K. A. Naugolnykh (2003), Crosswind ocean radar backscatter and two-scale scattering model at low grazing angles, *Radio Sci.*, *38*(3), 8037, 1–8.
Soriano, G., C. Guérin, and M. Saillard (2002), Scattering by two-dimensional rough surfaces: Comparison between the method of moments, Kirchhoff and small-slope approximations, *Waves Random Media*, *12*(1), 63–84.
Tanelli, S., S. L. Durden, and E. Im (2006), Simultaneous measurements of Ku- and Ka-band sea surface cross sections by an airborne radar, *IEEE Geosci. Remote Sens. Lett.*, *3*, 359–363, doi:10.1109/LGRS.2006.872929.
Tsai, W.-T., and L.-P. Hung (2007), Three-dimensional modeling of small-scale processes in the upper boundary layer bounded by a dynamic ocean surface, *J. Geophys. Res.*, *112*, C02019, doi:10.1029/2006JC003686.
Tsai, W.-T., and L.-P. Hung (2010), Enhanced energy dissipation by parasitic capillaries on short gravity-capillary waves, *J. Phys. Oceanogr.*, *40*(11), 2435–2450.
Ulaby, F. T., M. W. Whitt, and K. Sarabandi (1990), AVNA-based polarimetric scatterometers, *IEEE Antennas Propag. Mag.*, *32*(5), 6–17.
Vandemark, D., B. Chapron, J. Sun, G. Crescenti, and H. Graber (2004), Ocean wave slope observations using radar backscatter and laser altimeters, *J. Phys. Oceanogr.*, *34*(12), 2825–2842.
Walsh, E., D. Vandemark, C. Friehe, S. Burns, D. Khelif, R. Swift, and J. Scott (1998), Measuring sea surface mean square slope with a 36-GHz scanning radar altimeter, *J. Geophys. Res.*, *103*(C6), 12,587–12,601.
Walsh, E. J., M. L. Banner, C. W. Wright, D. C. Vandemark, B. Chapron, J. Jensen, and S. Lee (2008), The southern ocean waves experiment. Part III: Sea surface slope statistics and near-nadir remote sensing, *J. Phys. Oceanogr.*, *38*(3), 670–685, doi:10.1175/2007JPO3771.1.
Zavadsky, A., D. Liberzon, and L. Shemer (2013), Statistical analysis of the spatial evolution of the stationary wind wave field, *J. Phys. Oceanogr.*, *43*(1), 65–79.